Title: Oscillations support short latency co-firing of neurons during human episodic memory formation

Authors: Frédéric Roux[1], George Parish[1], Ramesh Chelvarajah[1,2], David T. Rollings[2], Vijay Sawlani[1,2,] Hajo Hamer[3], Stephanie Gollwitzer[3], Gernot Kreiselmeyer[3], Marije Ter Wal[1], Luca Kolibius[4], Bernhard Staresina[1,5], Maria Wimber[1,4], Matthew W. Self[6], Simon Hanslmayr*[1,4]

Affiliations:

[1]School of Psychology, University of Birmingham, Birmingham B15 2TT, United Kingdom
[2]Complex Epilepsy and Surgery Service, Neuroscience Department, Queen Elizabeth Hospital, Birmingham B15 2TH, United Kingdom
[3]Epilepsy Center, Department of Neurology, University Hospital Erlangen, 91054 Erlangen, Germany
[4]Institute of Neuroscience and Psychology, University of Glasgow, Glasgow G12 8QB, United Kingdom
[5] Department of Experimental Psychology, University of Oxford, Oxford, OX2 6GG, United Kingdom
[6] Department of Vision and Cognition, Netherlands Institute of Neuroscience, an institute of the Royal Netherlands Academy of Art and Sciences (KNAW), Amsterdam, the Netherlands

Abstract: Brain oscillations mediate efficient information transfer between neurons in animal models of memory. Theta and gamma oscillations in the medial temporal lobe are thought to establish short-latency co-firing of neurons to support memory formation. However, evidence for such a role of oscillations in human episodic memory has so far remained elusive. We recorded single unit activity and local field potentials in patients with epilepsy. The results show that phase coupling of neurons to faster theta and gamma oscillations correlates with co-firing at short latencies (~20-30 ms) and occurs during successful memory formation. Phase coupling at slower oscillations in these same frequency bands, by contrast, correlates with longer co-firing latencies and occurs during memory failure. A computational model using slow and fast theta/gamma oscillations demonstrates that faster oscillations yield more efficient synaptic plasticity. These results support the long-standing assumption that oscillations support episodic memory formation via establishing short-latency co-firing of neurons.

Main Text: Episodic memory relies on synaptic modifications transforming fleeting experiences into durable memory traces (*1*). The strengthening of synaptic connections between neurons that are active during the experience of an episode in turn critically depends on the temporal structure of neural firing (*2-5*). Evidence that has accumulated over several decades suggests that coordinated rhythmic activity may provide a candidate mechanism to impose a fine-grained temporal structure on neural firing (*6-8*). Accordingly, brain oscillations at theta (~3 – 9 Hz) and gamma (~ 40 – 80 Hz) frequencies in the human medial temporal lobe (MTL), a brain structure critical for memory (*9*), have been proposed to promote the formation of memories through the synchronization of neural firing in the MTL (*10-13*).

While it has long been assumed that correlated neural firing is fundamentally involved in the strengthening of synaptic connections (*4*) the mechanisms of memory formation in the human brain have remained largely unknown. Evidence suggests that synchronization of neurons to theta oscillations (*14*), as well as the presence of fast gamma oscillations (*15*) represent favorable conditions for human memory formation. However, so far, the role of theta and gamma oscillations in mediating neural co-firing in humans during memory formation has remained unclear. This study fills this gap by providing novel evidence of neural co-firing phase coupled to the frequency of theta and gamma oscillations recorded from micro-wire electrodes during an associative episodic memory task (Figure 1A). Our results show that successful memory formation is correlated with spike-LFP coupling at faster theta and gamma oscillations. Furthermore, we show that the power of gamma oscillations is coupled to the phase of theta oscillations specifically for successful memory trials, and that successful memory trials are characterized by short-latency co-firing of neurons. The mechanistic implications of the present findings for synaptic plasticity are illustrated by a computational model that highlights a functional role of neural oscillations in modulating neural co-firing and thus the strength of spike-timing-dependent-plasticity (STDP)(*3*).

Memory task and behavior

Nine patients with refractory epilepsy participated in 40 sessions of an associative episodic memory task (Figure 1A). During the encoding phase of the task, the patient was presented with several trials each containing a picture of an animal (cue), which was shown for 2 seconds. Then a pair of images appeared which either showed a face and a place, two faces or two places. The patients were instructed to link the three elements of the episode together by mentally imagining a narrative (e.g. “I saw a tiger in the zoo with Stephen Fry”) and press a button to indicate whether the invented narrative or combination of images was plausible or implausible, then the next trial followed. After the encoding phase and a brief distractor test, memory performance was assessed by means of a cued recall test. During the test phase the picture of the animal was presented for 2 seconds and the patient indicated how many stimuli they could remember (0, 1 or 2). Then a screen with four images appeared, and the patient selected the two images that they thought were paired with the cue originally. Trials for which both images were correctly recalled are labelled ‘hit’, all other trials (i.e. 1 image or both wrong) are labelled ‘miss’. Therefore, contrasting hits with misses isolates neural processes which support the complete memorization of an episode (as opposed to incomplete memories or no memory at all). Any such process has to start when the full memory information is present, which is at the onset of the face/place images (i.e. 2 seconds). Therefore, all subsequent analysis focused on this time window (2-3 seconds; highlighted in Figure 1A).

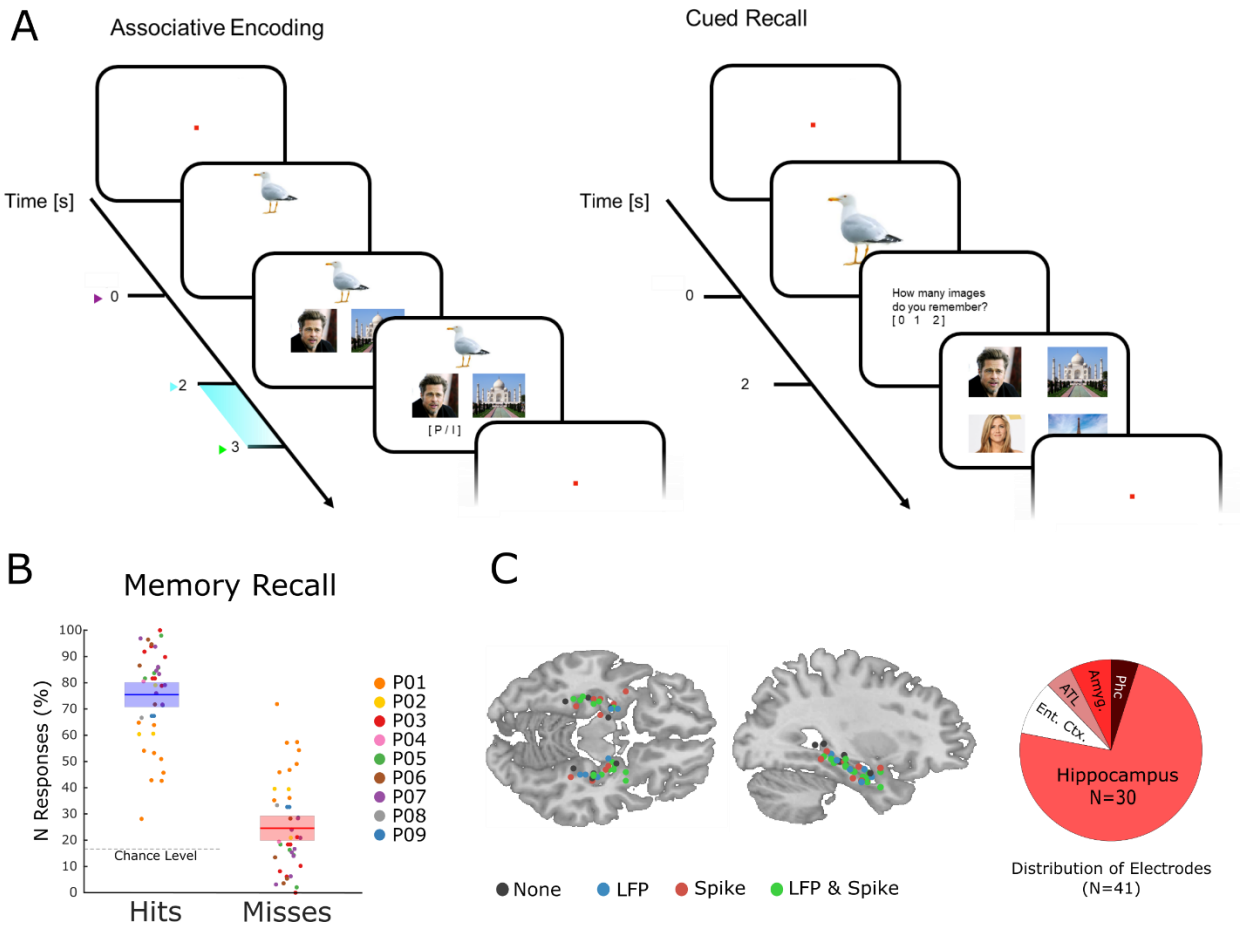

Figure 1. The memory task and behavioral results. (A) During encoding patients had to memorize triplets of stimuli consisting of an animal, and a face and a place (or two faces, or two places). The light blue bar highlights the time that was used for analysis. (B) Memory performance during the cued recall test is shown for all patients and sessions. Note that chance level is 16.6%. (C) Electrode locations are plotted overlaid onto a template brain in MNI space. Color codes indicate whether an electrode provided LFP, Spiking, both, or no data. The pie chart on the right shows the distribution of electrodes across MTL regions (Ent. Ctx.: Entorhinal Cortex; ATL.: Anterior Temporal Lobe; Amyg.: Amygdala; Phc.: Parahippocampal Cortex).

On average patients correctly recalled both associated items on 75.43% (s.d.: 13.3) of the trials (Figure 1B). Note that this is well above chance level (16.6%). The remaining miss trials were approximately evenly distributed between incomplete memories (i.e. only one association recalled; 12.6%) or completely forgotten (i.e. both incorrect; 11.9%).

Within-region spike-LFP coupling to fast gamma oscillations correlates with memory

Neural spiking and LFP activity were recorded with Behnke-Fried hybrid depth-electrodes from MTL regions (Figure 1C). Most electrodes (73%) were located in the hippocampus, the rest was located in adjacent MTL regions. Altogether 232 putative single and multi-units were recorded, of which 218 were used for further analysis (14 units were rejected because of too low firing rates; see Supplementary Methods). Neural firing during encoding was not modulated by memory for the time window of interest (2-3 seconds). However, hits showed a sustained increase in firing rate compared to misses at a later time window (>3 seconds; Figure S1). LFPs for hits and misses also

did not differ in terms of event-related potentials or inter-trial phase coherence (Fig. S2, S3C-D), but showed expected differences in broad band power (*16*), with hits showing decreased low frequency but increased high frequency power (Fig. S3A-B).

Synchronization of neural firing of an individual neuron to the population activity can be measured with spike-field coupling (SFC). SFC can occur at two different spatial levels, locally (within a region) or distally (across regions; see Supplementary Methods; Figure 2A). Locally, SFC indicates the firing of a neuron being entrained to its surrounding LFP. Distally, SFC likely indicates that the firing of one neuron elicits post-synaptic currents in another region. Because postsynaptic currents reflect the aggregated input to a neuron, distal spike-field coupling is usually interpreted as a functional measure of connectivity, with the spike providing region being the up-stream sender, and the LFP providing region being the down-stream receiver (*17-19*). Accordingly, we split spike-LFP pairs into these two categories, i.e. local and distal couplings. SFC was measured with the pairwise phase-consistency index (PPC)(*20*), which was preferred over other measures because it is not biased by the number of observations (e.g., spikes, trials).

During the time window of interest (2-3 seconds), 192 significantly (Rayleigh test; $p_{corr}<0.05$; FDR-correction) coupled spike-LFP pairs were found in the high-frequency range (40-80 Hz), of which 53 were coupled to the local LFP and 139 coupled to distal LFPs (Figure 2A). The number of locally coupled pairs was significantly higher than chance (Randomization test; $p<0.0001$), whereas the number of distally coupled pairs was not ($p>0.5$). Local spike-field coupling showed a pronounced peak in the fast gamma range (~65 Hz), which was substantially stronger compared to distal couplings (T-test; $p_{corr}<0.05$; Figure 2B; FDR-correction). Importantly, the peak frequency of local spike-field coupling varied as a function of memory formation such that hits showed stronger spike-field coupling at a higher frequency (~70 Hz) than misses (~62 Hz; T-test; $p_{corr}<0.05$; FDR-correction; Figure 2C). This effect was also significant when using sessions as random variable (T-test; $t_{19}=2.21$; $p<0.05$).

This pattern suggests a shift in frequency, with hits showing spike-field coupling at a higher gamma frequency compared to misses. To test whether this shift of gamma frequency occurred consistently across spike-LFP pairs a peak detection analysis was conducted where gamma peak frequencies for hits and misses were extracted and compared for each pair. The results confirmed that hits were characterized by significantly faster gamma frequencies compared to misses (T-test; $t_{36}=1.96$; $p<0.05$; Figure 2D). Figure 2E shows this effect for one example unit, which couples to a slightly slower gamma rhythm for misses compared to hits. A control analysis, which effectively controls for a possible selection bias due to unbalanced trial numbers revealed similar results (Figure S4B).

A set of control analyses were carried out to address possible concerns about non-stationarity of the signal (see Supplementary Methods). First, we carried out a series of simulations to ensure that the Wavelet filters used here yield correct phase estimates for non-stationary signals (Fig. S5). Second, we repeated the analysis using a Hilbert transform instead of a Wavelet transform in combination with a bandpass filter (band-width of 4 Hz for theta and 8 Hz for gamma; see Fig S6). We also analyzed the power spectra of the LFP signal at spike times to ensure the presence of a meaningful physiological signal in the phase providing LFP signal (Fig. S7A-C), albeit this is not strictly needed for obtaining meaningful spike-LFP coupling results (*21, 22*). Finally, we tested whether the absolute amount of spike-LFP coupling differed between hits and misses by comparing peak PPC values between hits and misses. No significant differences in peak PPCs

were observed for the raw PPC values (T-test; t_{36}=-1.7098; p>0.05) and the selection-bias controlled data (T-test; t_{36}=1.135; p>0.25).

Taken together, the phase of fast gamma oscillations temporally organizes spikes within a region. Later fully remembered episodes (hits) are distinguished from incomplete or forgotten episodes (misses) by the frequency to which spikes are coupled to; with fast gamma oscillations benefiting memory formation, and slow gamma oscillations being detrimental for memory formation. This effect is unlikely to be caused by differences in stimulus evoked activity since neither ERPs nor firing rates showed a memory related difference in the time window of interest (Fig. S2-S3).

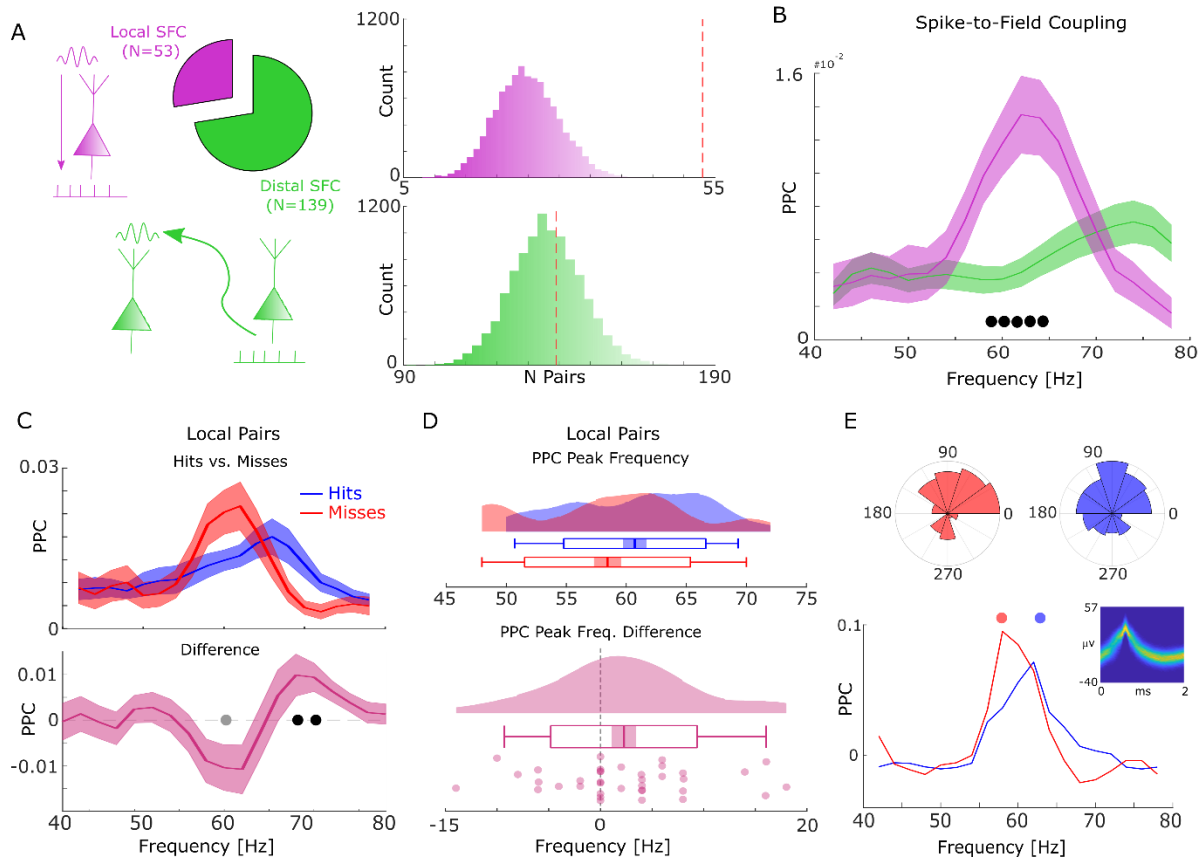

Figure 2. Spike-field coupling results for gamma. (A) Number of significant (p_{corr}<0.05) locally (pink) and distally (green) coupled spike-field pairs are shown. The histograms on the right show the results of a randomization procedure testing how many pairs would be expected under the null hypothesis. (B) Pairwise phase consistency (PPC) is plotted for local and distal spike-field pairs. Filled circles indicate significant differences (p_{corr}<0.05). Shaded areas indicate standard error of the mean. (C) Pairwise phase consistency (PPC) is shown separately for hits and misses (top panel), and for the difference between the two conditions (bottom panel) for locally coupled spike-field pairs. Filled black circles indicate significant differences (p_{corr}<0.05). Grey circles indicate statistical trends (p_{uncorr}<0.05). Shaded areas indicate standard error of the mean. (D) Peak frequency in PPC across all spike-field pairs is shown for hits and misses (top), and for the difference (hits-misses, bottom). The solid bar indicates the mean, shaded areas indicate standard error, the box indicates standard deviation, and the bars indicate 5th and 95th percentiles. (E) Local gamma spike-field coupling is shown for one example putative multi-unit recorded from the entorhinal cortex. Phase histograms on top indicate phase distribution for hits at 62 Hz (blue) and misses at 58 Hz (red). Spike wave shapes on the right are plotted by means of a 2D histogram.

Cross-regional Spike-LFP coupling to fast theta oscillations correlates with memory

The same spike-field coupling analysis as above was carried out for the low frequency ranges (2 – 40 Hz). We identified 103 locally coupled, and 387 distally coupled spike-field pairs (Rayleigh-test; $p_{corr}<0.05$; FDR corrected; Figure 3A). For both local and distal couplings the number of significant pairs exceeded chance level (Randomization test; both $p<0.0001$). Local couplings showed a peak PPC at around 5 Hz (and another peak at 13 Hz), whereas distal couplings showed a peak at around 8-9 Hz (Figure 3B). Local spike-field couplings were robustly stronger than distally coupled pairs in the beta frequency range (20-30 Hz).

For local spike-LFP coupling no significant differences ($p_{uncorr}>0.05$) between hits and misses were observed for the low frequency range. In contrast, distally coupled spike-field pairs showed stronger coupling for hits compared to misses in the fast theta frequency range (8-10 Hz) and higher spike-field coupling for misses compared to hits in the slower theta frequency range (5 Hz; Figure 3C, T-test; $p_{corr}<0.05$; FDR-corrected). The stronger spike-field coupling in the fast theta band for hits compared to misses was also found to be significant when using sessions (T-test; $t_{20}=3.25$; $p<0.005$) as random variable. No significant differences between hits and misses were obtained for locally coupled spike-field pairs.

Like the memory related difference in gamma peak frequency, a shift in peak frequency also drove the memory-related difference in distal theta spike-field coupling. This was confirmed by a peak detection analysis showing that hits exhibited a slightly faster peak in theta spike-field coupling compared to misses (T-test; $t_{206}=3.49$; $p<0.0001$; Figure 3D). This effect is shown for one example unit which is distally coupled to a slow theta oscillation for misses, and to a fast theta oscillation for hits (see Figure S4A for control analysis on selection bias). As for gamma, control analyses addressing concerns about non-stationarity of the signal and the existence of meaningful theta power in the phase providing LFP signal are shown in Fig. S5-S7. Like the effects in local gamma coupling these effects are unlikely to be due to changes in stimulus evoked activity (Fig. S2-S3), and/or due to theta rhythmicity in the spiking of neurons themselves (Fig. S8).

To assess the direction of information flow of distal theta spike-LFP coupling, and to test whether this flow of information has any bearing on memory performance, we compared the Phase Slope Index (PSI) between hits and misses. Positive values indicate that the spike providing signal is the sender and the LFP providing signal is the receiver and vice versa. The results indicate above chance PSIs for hits peaking in the high theta band (7-8 Hz). In addition, hits show significantly higher PSIs compared to misses (Fig. 4), whereas PSIs for misses do not differ from zero.

In agreement with the results obtained for local gamma oscillations we observed that distal theta spike-LFP coupling varied as a function of memory formation, with hits showing spike coupling at faster theta peak frequencies compared to misses. Thus, the present findings reveal two distinct cell populations that synchronize either to local gamma rhythms or distal theta rhythms, and a functional relationship between the peak frequency of gamma and theta phase coupling and memory formation. Importantly, directional coupling analyses demonstrate that the spike providing signal is the upstream sender and the LFP providing signal is the downstream receiver. This result likely does not indicate that one single neuron can drive the entire LFP in a receiving region. Instead, it likely indicates that the spikes of a large population of neurons, of which we happen to sample one, provide input to a receiving region. This direction of information flow was dependent on memory success, suggesting that successful memory formation correlates with efficient cross-regional information transfer.

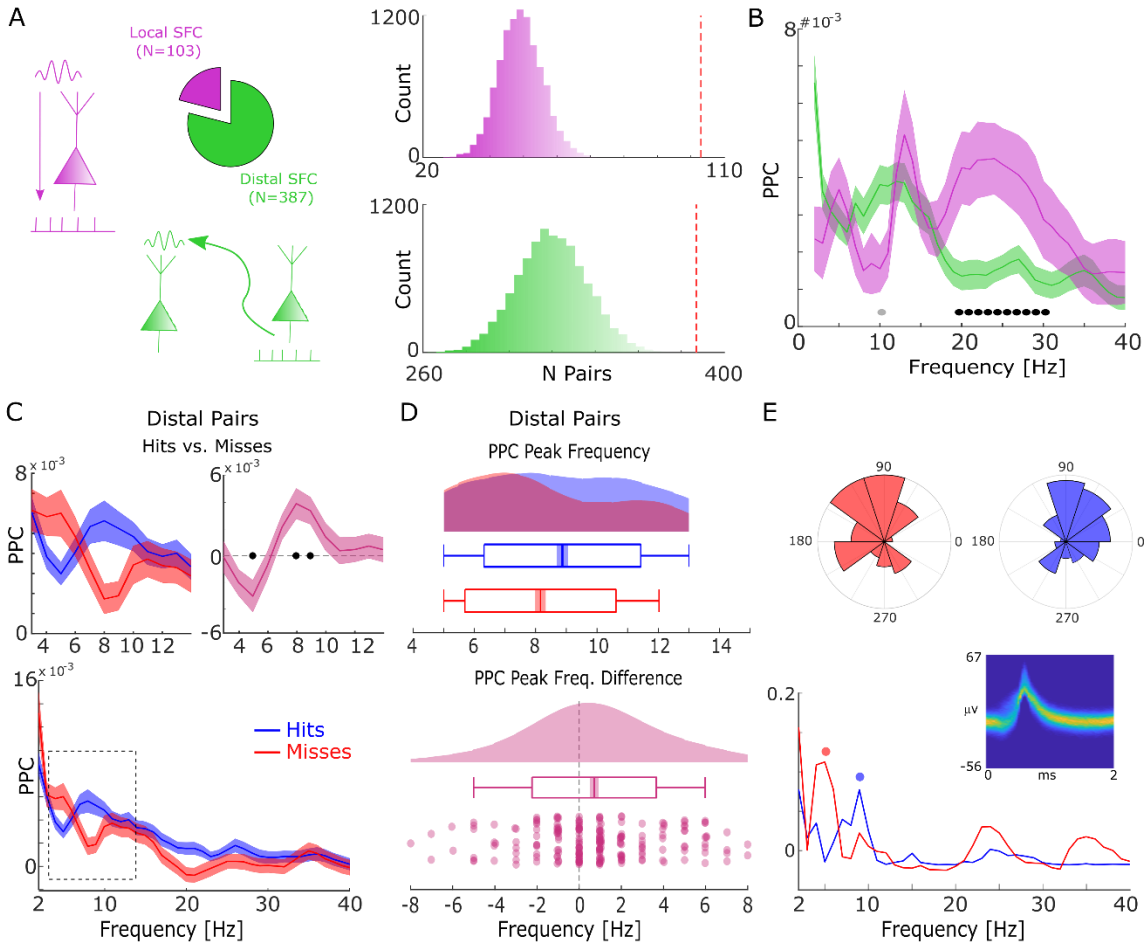

Figure 3. Spike-field coupling results for the lower frequencies. (A) Number of significant (p_{corr}<0.05) locally (pink) and distally (green) coupled spike-field pairs are shown. The histograms on the right show the results of a randomization procedure testing, with the red dashed line indicating the empirically observed value. (B) PPC is plotted for local and distal spike-field pairs. Filled circles indicate significant differences (p_{corr}<0.05). Grey circles indicate trends (p_{uncorr}<0.05). Shaded areas indicate standard error of the mean. (C) PPC is shown separately for hits (blue) and misses (red), and for the difference between the two conditions (magenta) for distally coupled spike-field pairs. The top panels show PPC values for the theta frequency range, the bottom panel shows all frequencies up to 40 Hz. Shaded areas indicate standard error of the mean. Filled circles indicate significant differences (p_{corr}<0.05). (D) Peak frequency in PPC across all distal spike-field pairs is shown for hits and misses (top), and for the difference (hits-misses). Box plots indicate the same indices as in Fig 2D. (E) Distal theta spike-field coupling is shown for one example unit recorded from the left posterior hippocampus, and the LFP recorded from the left entorhinal cortex. Phase histograms on top indicate phase distribution for hits at 9 Hz (blue) and misses at 5 Hz (red). Spike wave shapes on the right are plotted by means of a 2D histogram.

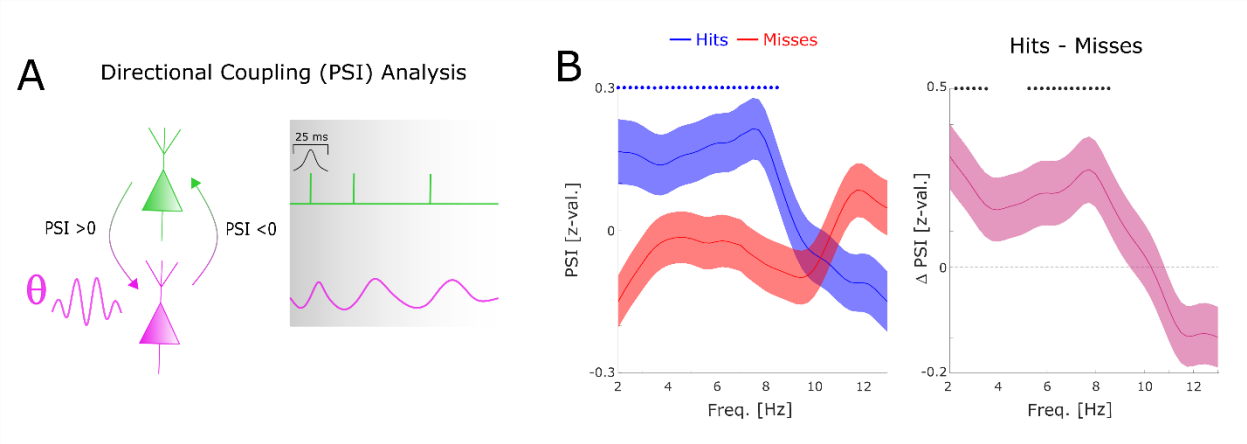

Figure 4. Directional coupling analysis of distal spike-LFP coupling using Phase Slope Index (PSI). A) A schematic of the analysis is shown. Spike time series were convolved with a gaussian window, and the PSI was calculated between the spike time series (green) and the distally coupled LFP (pink). B) The left plot shows normalized PSI (i.e. z-values) for hits (blue) and misses (red). Hits show significantly positive PSIs throughout the theta frequency range, peaking at ~ 8 Hz (blue dots; $p_{corr} < 0.05$). The right plot shows the difference in PSI between hits and misses. Hits show significantly higher PSIs compared to misses, especially in the high theta range (black dots; $p_{corr}<0.05$).

Theta and gamma oscillations are coupled for hits but not for misses

The above results show that successful memory formation relies on gamma oscillations synchronizing neurons at a local level, and theta oscillations at ~8 Hz synchronizing neurons across regions. Intriguingly, peak frequencies of both oscillations showed a similar relationship with memory formation, with faster frequencies being associated with successful memory. This raises the question of whether gamma and theta oscillations are also temporally coordinated. For this analysis we considered electrodes from regions where the LFP was locally coupled to spikes in the gamma range and distally coupled to spikes in the low frequency (theta) range. More than half of the electrodes (58%) were available for this analysis (Figure 5A). Cross-frequency coupling was calculated by means of phase-amplitude coupling using the modulation index (*23*). Importantly, theta and gamma frequencies were adjusted to their peak frequency for each condition to account for the systematic difference in peak frequencies between hits and misses and to ensure the presence of a physiologically meaningful oscillation in both conditions (*24*)(see also Fig. S7). Theta phase to gamma power coupling was evident in single trials (Figure 5B-C). Hits showed stronger theta phase to gamma amplitude coupling compared to misses (Figure 5D; Wilcoxon test; $z=3.7$; $p<0.00001$). This increased cross-frequency coupling for hits compared to misses was also significant when pooling the data across sessions (Wilcoxon test; $p<0.05$). Cross-frequency coupling can be subject to several confounds, which we addressed by a series of control analyses (Supplementary Material and Fig. S9).

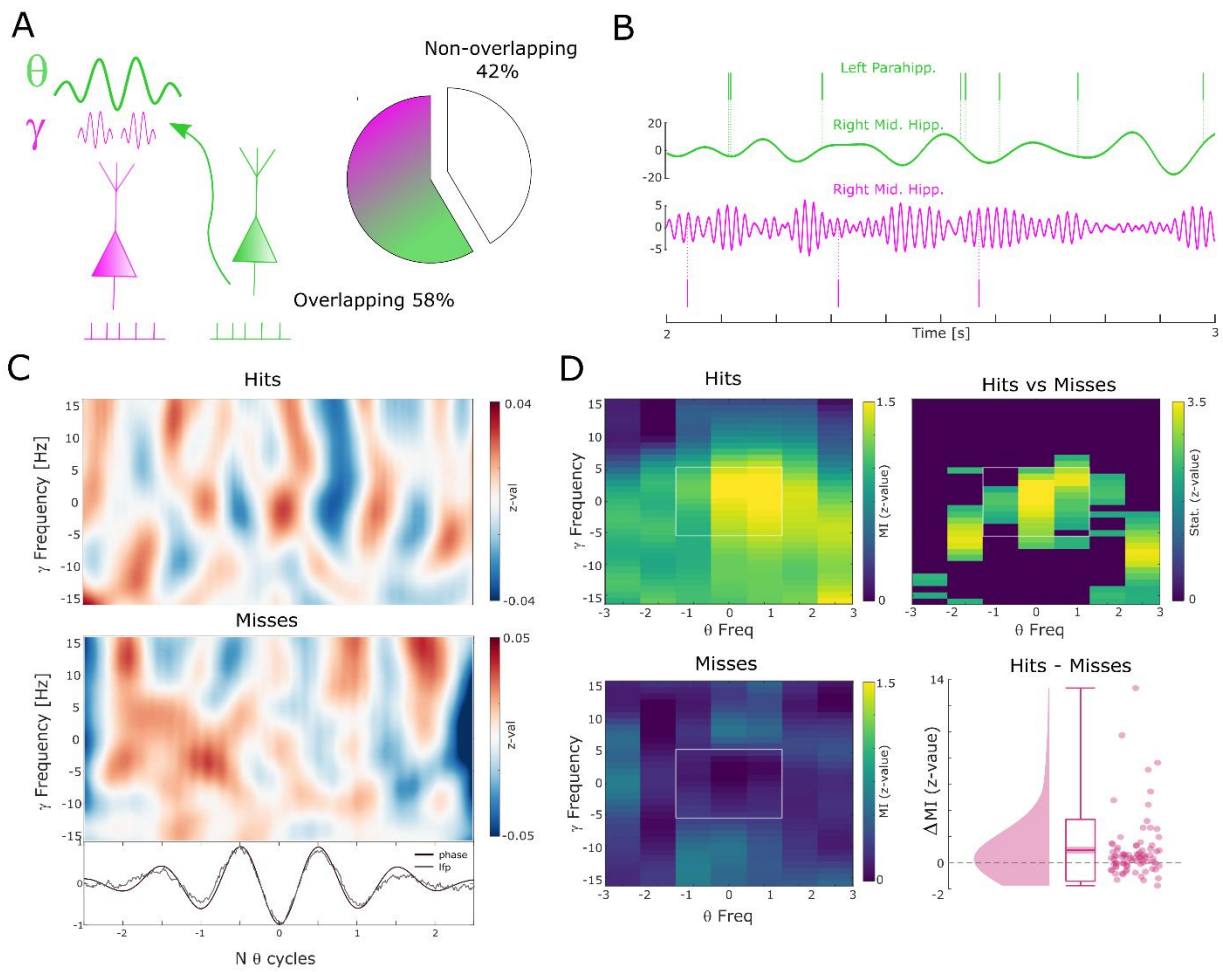

Figure 5. Theta to gamma cross frequency coupling results. (A) Percentage of overlapping local gamma (pink) and distal theta (green) spike-field pairs are shown. (B) Spikes and band-pass filtered LFP data for one example single trial are shown. The top row shows spikes from a unit in the left parahippocampal cortex which are coupled to the LFP in the right middle hippocampus (green). The gamma LFP from the same region (right mid hippocampus) is shown below (pink) as well as spikes from a unit in the same region that is coupled to this gamma oscillation. Note the gamma power increase around theta troughs. (C) Theta phase sorted gamma power (y-axis centered to gamma peak frequency) is shown for all trials for the data shown in (B). The bottom panel shows averaged normalized band-pass filtered LFP data (black) and unfiltered LFP data (grey). (D) Co-modulograms are shown for hits and misses. Modulations indices(*23*), which indicate the strength of cross-frequency coupling, are plotted in terms of z-values where means and standard deviations were obtained from a trial shuffling procedure. The difference between hits and misses is shown as z-values obtained from a non-parametric Wilcoxon signrank test masked with $p_{corr}<0.05$ (FDR-corrected). The panel in the bottom right shows the individual differences between hits and misses across the whole dataset (N=83 pairs).

Short co-firing latencies predict successful memory formation

Brain oscillations have been proposed to establish efficient communication between neural ensembles (*7*), with faster frequencies reflecting tighter synchronization of spikes. The effect on a downstream neuron of such a tighter synchronization upstream is that it is more likely to fire at all, and more likely to fire at an earlier time point (*6*). This can be demonstrated by considering two neurons which both have the same preferred phase of firing (e.g. maximal excitation), and which are both coupled by an oscillation with a constant phase lag of pi/4 (with neuron 1 leading

and neuron 2 lagging). If the two neurons are coupled at a frequency of 8 Hz, then neuron 2 would fire ~31 milliseconds after neuron 1 (i.e. 8 Hz equals a period length of 125 ms, divided by 4 = 31.25). If the neurons are, however, coupled at 4 Hz then neuron 2 would fire ~62 milliseconds after neuron 1. Therefore, the faster theta and gamma oscillations observed for hits may reflect more efficient information transmission between theta-gamma coupled neural pairs. In order to test this hypothesis, we analyzed co-firing of neurons at different time lags by computing the cross-correlation of spike trains between theta up-stream units (i.e. the distally coupled unit) and their corresponding gamma down-stream unit (i.e. the locally coupled unit; Figure 6A). Overall, 32 pairs were available for this analysis, 24 of which showed above threshold co-firing (see Supplementary Methods). Cross-correlations for hits and misses were each compared to a trial-shuffled baseline and transformed to z-scores effectively eliminating biases introduced by different trial numbers.

Compared to baseline, hits showed significant above chance co-firing at lags 20-40ms, whereas co-incidences for misses peaked at 60 ms (T-test; $p_{corr}<0.05$; FDR-correction; Figure 6B). In addition, hits showed stronger co-firing compared to misses at 20 ms (T-test; $p_{corr}<0.05$; FDR-correction; Figure 6B). A peak detection analysis revealed that co-firing for hits peaked significantly earlier compared to misses ($t_{21}=-3.2$; $p<0.005$; Figure 6D). This result held also when using a more conservative approach, i.e., pooling the data across number of neurons ($t_{11}=-3.34$; $p<0.01$). Intriguingly, this memory related co-firing effect was observed only when selecting pairs of neurons that were both locally coupled to gamma, and distally coupled to theta. Analyzing all possible pairs of distally coupled theta units showed no differences in peak co-incidences between hits and misses ($t_{126}=-0.78$; $p>0.4$). This is quite remarkable given that statistical power for this latter analysis was substantially higher. This pattern of results suggests that the coupling of down-stream neurons to local fast gamma oscillations is crucial for observing the memory dependent effect of co-firing at critical time windows. In order to test for a similar effect in the reverse direction (i.e. local gamma coupled neuron --> distal theta coupled neuron) the same co-incidence analysis was carried out for negative lags. Intriguingly, misses showed peak co-firings at shorter negative latencies (i.e. closer to 0) compared to hits (Fig. S10; $t_{20}=-2.82$; $p<0.05$). This result is consistent with the STDP framework, whereby a negative time lag leads to a decrease of synaptic connectivity (*2, 3*)

Together, these results suggest that successful memory formation correlates with shorter latencies of co-firing between down-stream and up-stream neurons. Notably, this effect is selective for neuron pairs that are both distally theta coupled and locally gamma coupled.

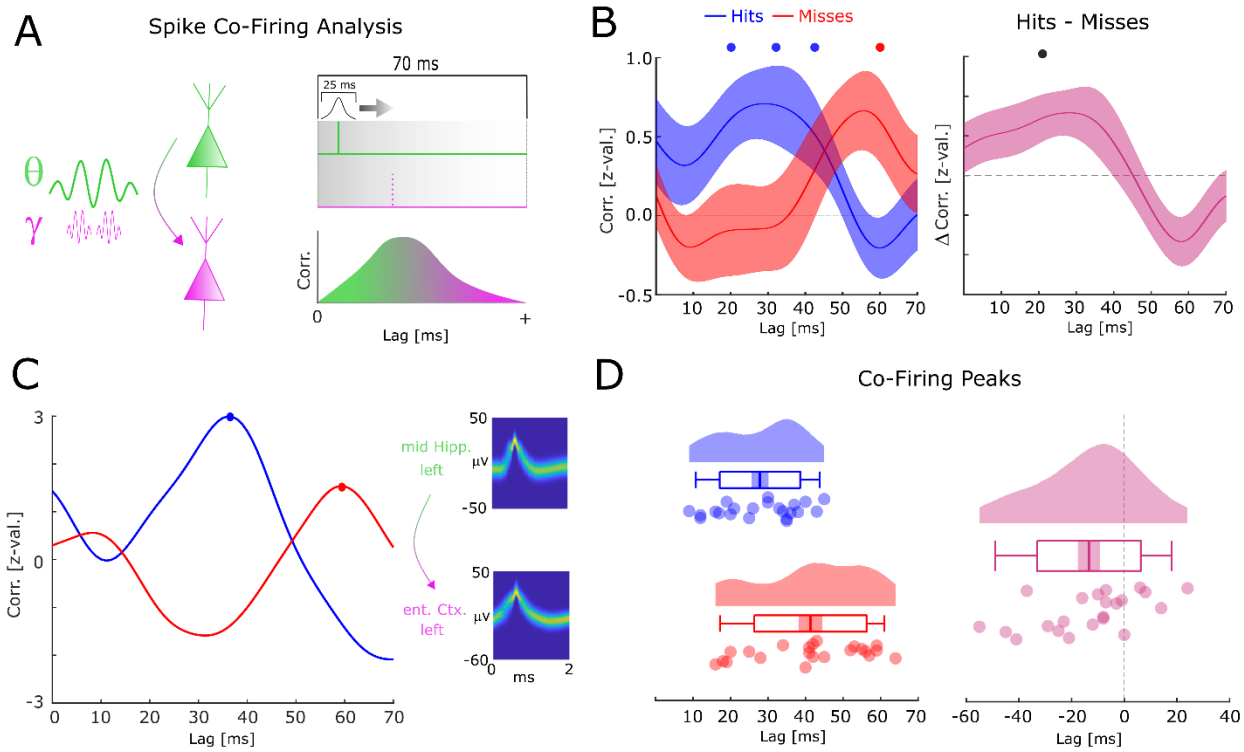

Figure 6. Co-firing analysis results for theta-gamma coupled assemblies. (A) A schematic of the co-firing analysis is shown. Pairs of putative up-stream (green) and putative down-stream (pink) units were selected for the co-firing analysis. Co-firing was measured by cross-correlating spike time series (convolved with a Gaussian envelope). Cross-correlations indicate the latency of firing of a putative down-stream neuron (pink) in response to a putative up-stream neuron (green). (B) Spike cross-correlations for hits and misses are plotted in terms of z-values derived from a trial shuffling procedure. Hits (blue) show increased co-firing between putative up-stream and putative down-stream neurons at around 20-40 ms ($p_{corr}<0.05$), whereas misses (red) peak at 60 ms ($p_{corr}<0.05$). Shaded areas indicate standard error of the mean. Differences between co-firing of hits and misses is plotted on the right. Hits show higher co-firing at 20 ms compared to misses ($p_{corr}<0.05$). (C) Co-firing data is shown for one example pair of units. (D) Results of the co-firing peak detection analysis. The distribution of the peak lag is shown for hits (blue) and misses (red), and for the difference for each pair of neurons (pink). Hits exhibit significantly shorter lags of co-firing compared to misses ($p<0.005$).

Computational modelling of results in relation to synaptic plasticity

The above results suggest that successful memory formation is supported by a frequency shift of theta and gamma spike-LFP coupling (Figures 2 and 3), an increase in theta-to-gamma coupling (Figure 5), as well as shorter latencies of co-firing between putative up-stream and down-stream assemblies (Figure 6). Thus, we next examined if this shift in theta/gamma peak-frequency could lead to more efficient neural information transmission and increased synaptic plasticity. To address these questions, we explored the consequences of slower vs. faster rhythms on neural co-firing and synaptic plasticity in a computational model which simulated up-stream theta and down-stream gamma cell assemblies (Figure 7A) as observed in our data. Up-stream neurons were phase coupled to a theta rhythm and transmitted their activity to a down-stream assembly which in turn was locally phase coupled to a gamma rhythm. Hit trials were simulated by setting the theta

frequency to 9 Hz and the gamma frequency to 70 Hz; for miss trials theta was set to 5 Hz and gamma to 60 Hz. In addition, gamma amplitude to theta phase coupling was set to be higher for hits compared to misses.

Model behavior is shown for a successful (hit) trial and an unsuccessful (miss) trial in Figure 7B. The differences in theta and gamma frequencies are apparent in the raster plots showing a tighter packaging of spikes for the hit trial compared to the miss trial. This difference in frequency and theta-to-gamma coupling had a dramatic effect on synaptic plasticity as modeled by STDP, with the synaptic weights in the hits condition plateauing at a much faster rate than in the miss condition (Figure 7C). This figure also demonstrates that the model successfully replicated earlier co-firing for hits compared to misses (Figure 7C, bottom). Further analysis of the data showed that this difference in co-firing lag was not due to a change in the phase at which neurons fired (Fig. S11A-B) and hence can be attributed to the difference in frequencies between hit and miss trials.

Though we do not attempt to fully explain how these oscillations might arise in the brain, this simple simulation can demonstrate the potential impact that they might have on co-incidence of firing and plasticity processes. The observed correlation between the co-firing and synaptic plasticity in our computational model can be unequivocally attributed to the change in the peak frequencies of theta and gamma oscillation. Thus, the present results show that a shift in the peak frequency of theta and gamma oscillations directly affects synaptic plasticity. By evaluating the parameter space for theta vs gamma frequency by plasticity (see Fig. S12), the computational model further suggests that theta frequency might be the main driver of long-range distal-to-local synaptic plasticity, whilst gamma frequency might be the main driver of short-range local-to-local synaptic plasticity. This suggests that neural synchronization at fast theta and gamma frequencies could be an efficient one-shot learning mechanism underlying episodic memory formation (*12*).

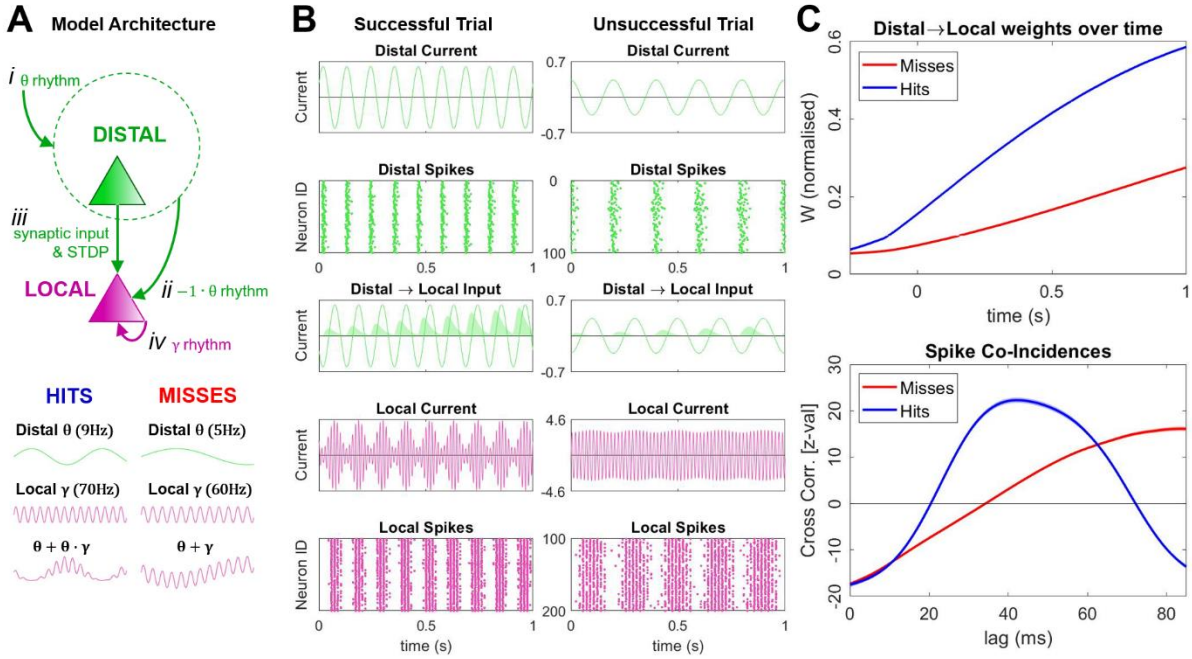

Figure 7. Computational model demonstrating the impact of slow/fast oscillations on spike-timing dependent plasticity (STDP). (A) Model architecture. A set of distal neurons (green) receive a θ-rhythm (i). This θ-rhythm filters through the hippocampus, resulting in a set of local neurons (purple) receiving a phase-reversed θ-rhythm (ii). Distal neurons connect to local neurons (iii), such that weighted distal spikes cause post-synaptic potentials in local neurons

and spike-timing-dependent-plasticity (STDP) increases these weights over time. Local neurons also receive a γ-rhythm that is modulated to some degree by the incoming θ-rhythm (iv). For "hits" (blue), distal θ-frequency is 9Hz and γ-frequency is 70Hz, with a high degree of θ:γ cross-frequency coupling. For "misses" (red), distal θ-frequency is 5Hz and γ-frequency is 60Hz, with a low degree of θ:γ cross-frequency coupling. (B) A simulation of a single trial through time for "hits" (left) and "misses" (right). The amplitude of a distal θ-rhythm (top panel) causes spike events in distal neurons (2nd top panel). Distal spike events then induce post-synaptic potentials in local neurons (middle panel; green shaded), which, alongside a phase-reversed θ-rhythm (middle panel; green line), summarizes distal output to local neurons. These operate in conjunction with a locally entrained θ:γ-rhythm (2nd bottom panel) to cause spike events in local neurons (bottom panel). (C) STDP acts to increase the weights of distal to local synapses through time for the "hits" condition (blue). This is a much slower process for the "misses" condition (red), indicating the positive correlation between oscillatory frequency and learning in human episodic memory. This is corroborated by the spike co-incidences between distal and local spike pairings (bottom panel) where local spikes are more likely to occur shortly after a distal spike for the "hits" condition (blue), thus increasing the likelihood of STDP operating on the active synapse.

Conclusions

More than seven decades ago Donald Hebb proposed the idea that "neurons that fire together, wire together" (*4*). He argued that correlated neural firing plays a crucial role for laying down the neural connections that make up a memory. Although this principle has been well established by animal studies (*2, 3, 5*), a direct correlation between co-firing of neurons and memory formation has so far not been demonstrated in the human brain. The present study provides critical support for Hebbian learning in the human medial temporal lobe in showing that co-firing of neurons at short latencies is correlated with the formation of episodic memories in neurons that are synchronized by local gamma and distal theta oscillations. Furthermore, our study demonstrates that co-firing at shorter lags is associated with a coupled upward shift in spike-LFP coupling peak frequency of gamma and theta oscillations. Using a computational model we can demonstrate that the observed results are consistent with prominent synaptic plasticity mechanisms, such as STDP (*3*).

Although our study provides critical new insights into the role of oscillations in mediating neural synchrony and memory formation important questions remain. For instance, does the neural co-spiking reflect the synchronization of neurons that actually belong to the engram that encode the episode? Or, does it instead reflect a more general process that is conducive for episodic memory formation? At this stage we cannot disambiguate between these two possibilities, however, the fact that the here described neurons demonstrate more general firing rate (Fig. S1) and synchronization effects for hits compared to misses would be consistent with the latter account (i.e. a general memory process). Further experiments are needed to investigate this question in detail.

Acknowledgments

We like to thank all patients for taking time to participate in the experimental sessions. We also thank Markus Siegel for providing useful comments on previous versions of the manuscript and Pieter Roelfsema for supporting us with data collection. S.H. was supported by grants from the European Research Council (Nr. 647954), and the Economic and Social Research Council (ES/R010072/1). M.tW. and M.W. were supported by a grant from the European Research Council (StG-715714).

References and Notes

Aru, J., Aru, J., Priesemann, V., Wibral, M., Lana, L., Pipa, G., Singer, W., and Vicente, R. (2015). Untangling cross-frequency coupling in neuroscience. Curr Opin Neurobiol *31*, 51-61.

Belluscio, M.A., Mizuseki, K., Schmidt, R., Kempter, R., and Buzsaki, G. (2012). Cross-frequency phase-phase coupling between theta and gamma oscillations in the hippocampus. J Neurosci *32*, 423-435.

Benjamini, Y., and Hochberg, Y. (1995). Controlling the False Discovery Rate - a Practical and Powerful Approach to Multiple Testing. J R Stat Soc B *57*, 289-300.

Bi, G., and Poo, M. (2001). Synaptic modification by correlated activity: Hebb's postulate revisited. Annu Rev Neurosci *24*, 139-166.

Brainard, D.H. (1997). The psychophysics toolbox. Spatial vision *10*, 433-436.

Burke, J.F., Ramayya, A.G., and Kahana, M.J. (2015). Human intracranial high-frequency activity during memory processing: neural oscillations or stochastic volatility? Curr Opin Neurobiol *31*, 104-110.

Burke, J.F., Zaghloul, K.A., Jacobs, J., Williams, R.B., Sperling, M.R., Sharan, A.D., and Kahana, M.J. (2013). Synchronous and asynchronous theta and gamma activity during episodic memory formation. J Neurosci *33*, 292-304.

Bush, D., and Burgess, N. (2020). Advantages and detection of phase coding in the absence of rhythmicity. Hippocampus *30*, 745-762.

Buzsaki, G. (2010). Neural syntax: cell assemblies, synapsembles, and readers. Neuron *68*, 362-385.

Buzsaki, G., and Schomburg, E.W. (2015). What does gamma coherence tell us about inter-regional neural communication? Nat Neurosci *18*, 484-489.

Eliav, T., Geva-Sagiv, M., Yartsev, M.M., Finkelstein, A., Rubin, A., Las, L., and Ulanovsky, N. (2018). Nonoscillatory Phase Coding and Synchronization in the Bat Hippocampal Formation. Cell *175*, 1119-1130 e1115.

Fell, J., and Axmacher, N. (2011). The role of phase synchronization in memory processes. Nat Rev Neurosci *12*, 105-118.

Fries, P. (2015). Rhythms for Cognition: Communication through Coherence. Neuron *88*, 220-235.

Griffiths, B., Parish, G., Roux, F., Michelmann, S., van der Plas, M., Kolibius, L., Chelvarajah, R., Rollings, D.T., Sawlani, V., Hamer, H., *et al.* (2019). Directional coupling of slow and fast hippocampal gamma with neocortical alpha/beta oscillations in human episodic memory. Proc Natl Acad Sci U S A *in press*.

Hebb, D.O. (1949). The organization of behavior; a neuropsychological theory (New York,: Wiley).

Hipp, J.F., Hawellek, D.J., Corbetta, M., Siegel, M., and Engel, A.K. (2012). Large-scale cortical correlation structure of spontaneous oscillatory activity. Nat Neurosci *15*, 884-890.

Huerta, P.T., and Lisman, J.E. (1995). Bidirectional synaptic plasticity induced by a single burst during cholinergic theta oscillation in CA1 in vitro. Neuron *15*, 1053-1063.

Hyman, J.M., Wyble, B.P., Goyal, V., Rossi, C.A., and Hasselmo, M.E. (2003). Stimulation in hippocampal region CA1 in behaving rats yields long-term potentiation when delivered to the peak of theta and long-term depression when delivered to the trough. J Neurosci *23*, 11725-11731.

Ison, M.J., Quian Quiroga, R., and Fried, I. (2015). Rapid Encoding of New Memories by Individual Neurons in the Human Brain. Neuron *87*, 220-230.

Jacob, S.N., Hahnke, D., and Nieder, A. (2018). Structuring of Abstract Working Memory Content by Fronto-parietal Synchrony in Primate Cortex. Neuron *99*, 588-597 e585.

Jacobs, J., Kahana, M.J., Ekstrom, A.D., and Fried, I. (2007). Brain oscillations control timing of single-neuron activity in humans. J Neurosci *27*, 3839-3844.

Jutras, M.J., and Buffalo, E.A. (2010). Synchronous neural activity and memory formation. Curr Opin Neurobiol *20*, 150-155.

Kandel, E.R. (2001). The molecular biology of memory storage: a dialogue between genes and synapses. Science *294*, 1030-1038.

Liebe, S., Hoerzer, G.M., Logothetis, N.K., and Rainer, G. (2012). Theta coupling between V4 and prefrontal cortex predicts visual short-term memory performance. Nat Neurosci *15*, 456-462, S451-452.

Markram, H., Lubke, J., Frotscher, M., and Sakmann, B. (1997). Regulation of synaptic efficacy by coincidence of postsynaptic APs and EPSPs. Science *275*, 213-215.

Niediek, J., Bostrom, J., Elger, C.E., and Mormann, F. (2016). Reliable Analysis of Single-Unit Recordings from the Human Brain under Noisy Conditions: Tracking Neurons over Hours. PLoS One *11*, e0166598.

Nolte, G., Ziehe, A., Nikulin, V.V., Schlogl, A., Kramer, N., Brismar, T., and Muller, K.R. (2008). Robustly estimating the flow direction of information in complex physical systems. Phys Rev Lett *100*, 234101.

Oostenveld, R., Fries, P., Maris, E., and Schoffelen, J.M. (2011). FieldTrip: Open source software for advanced analysis of MEG, EEG, and invasive electrophysiological data. Comput Intell Neurosci *2011*, 156869.
Penfield, W., and Milner, B. (1958). Memory deficit produced by bilateral lesions in the hippocampal zone. AMA Arch Neurol Psychiatry *79*, 475-497.
Quiroga, R.Q., Nadasdy, Z., and Ben-Shaul, Y. (2004). Unsupervised spike detection and sorting with wavelets and superparamagnetic clustering. Neural Comput *16*, 1661-1687.
Rutishauser, U., Ross, I.B., Mamelak, A.N., and Schuman, E.M. (2010). Human memory strength is predicted by theta-frequency phase-locking of single neurons. Nature *464*, 903-907.
Sederberg, P.B., Schulze-Bonhage, A., Madsen, J.R., Bromfield, E.B., McCarthy, D.C., Brandt, A., Tully, M.S., and Kahana, M.J. (2007). Hippocampal and neocortical gamma oscillations predict memory formation in humans. Cereb Cortex *17*, 1190-1196.
Singer, W. (1999). Neuronal synchrony: a versatile code for the definition of relations? Neuron *24*, 49-65, 111-125.
Tort, A.B., Komorowski, R., Eichenbaum, H., and Kopell, N. (2010). Measuring phase-amplitude coupling between neuronal oscillations of different frequencies. J Neurophysiol *104*, 1195-1210.
Vinck, M., van Wingerden, M., Womelsdorf, T., Fries, P., and Pennartz, C.M. (2010). The pairwise phase consistency: a bias-free measure of rhythmic neuronal synchronization. Neuroimage *51*, 112-122.
Wespatat, V., Tennigkeit, F., and Singer, W. (2004). Phase sensitivity of synaptic modifications in oscillating cells of rat visual cortex. J Neurosci *24*, 9067-9075.

Supplementary Materials for

Oscillations support short latency co-firing of neurons during human episodic memory formation

Frédéric Roux, George Parish, Ramesh Chelvarajah, David T. Rollings, Vijay Sawlani, Hajo Hamer, Stephanie Gollwitzer, Gernot Kreiselmeyer, Marije Ter Wal, Luca D. Kolibius, Bernhard P. Staresina, Maria Wimber, Matthew W. Self, Simon Hanslmayr

Correspondence to: simon.hanslmayr@glasgow.ac.uk

This PDF file includes:

Materials and Methods
Supplementary Text
Figs. S1 to S12
Table S1

Materials and Methods

Patients

Nine patients with refractory epilepsy volunteered to participate in the experiments. Mean age of patients was 37 years (s.d.: 9.1; range: 26-53). All but two patients were right handed. On average patients suffered 15.6 years from epilepsy. All patients had temporal lobe epilepsy with either a left (N=3), right (N=3) or bilateral focus (N=3). Each patient participated in at least one experimental session, and in most cases more than one session such that overall data from 40 sessions was available for analysis.

Patients were treated in one of three hospitals, the Queen Elizabeth University Hospital Birmingham (N=6), the Epilepsy Centre at the University Hospital in Erlangen (N=1), or the Vrije Universiteit Medisch Centrum Amsterdam (N=2). Ethical approvals were given by National Research Ethics Service (NRES), Research Ethics Committee (Nr. 15/WM/0219), the ethical review board of the Friedrich-Alexander Universität Erlangen-Nürnberg (Nr. 124_12 B), and the Medical Ethical Review board of the Vrije Universiteit Medisch Centrum (Nr. NL55554.029.15), for Birmingham, Erlangen and Amsterdam respectively.

Task and procedure

All participants completed at least one session of an associative episodic memory task which required patients to form trial unique associations between three images (Figure 1A). In one session, several blocks of the memory task were carried out. One block comprised of three phases, an encoding phase, a distractor phase and a recall phase. During encoding, participants were first presented with an image cue of an animal for 2 seconds, followed by a pair of 2 images made up of any combination of a well-known face or a well-known place (i.e., face–place, face–face, or place–place pairs; presented for 2 s). The initial number of trials was set according to the patient's cognitive abilities as estimated by the experimenter. This number was then reduced if the hit rate fell below 66.25%, or increased if the hit rate surpassed 73.75%, effectively adjusting task difficulty according to the participant's ability. On average, participants completed 19.1 trials (S.D.: 10.3; range: 2-82) per block. Participants were asked to vividly associate these triplets of images. Participants were encouraged to make up a story, which would link the three images to help them memorize the associations. For each triplet, participants were asked whether the story they came up with (or combination of pictures) was plausible or implausible. This plausibility judgment was used to keep participants on task rather than to yield a meaningful metric. Participants were self-paced in providing a judgment, and the following trial began immediately afterward. After encoding, the distractor phase was carried out which required participants to make odd/even judgments for 15 sequentially presented random integers, ranging from 1 to 99. Feedback was given after every trial. After completion of the distractor task, the retrieval phase commenced. Participants were presented with every animal image cue that was presented in the earlier encoding stage and, 2 s later, were asked how many of the associated face or place images they remembered (participants had the option of responding with 0, 1, or 2). If the participant remembered at least 1 image, they were then asked to select the pair of images from a panel of 4 images shown during the previous encoding block (2 targets and 2 foils). Foils were drawn from images, which were also presented in the preceding encoding phase but were paired with a different animal cue. Therefore, a given association could either be remembered completely (i.e. both images correctly identified), remembered partially (i.e. only one image

correctly identified), or fully forgotten (i.e. no image recalled or both incorrect). Participants were self-paced during the recall stage, though the experiment ended after a runtime of 40 min in total. All participants completed the task on a laptop brought to their bedside.

Recording Data

To record behavioural responses and to present instructions and stimuli, a Toshiba Tecra laptop (15.6 inch screen) was used in the hospitals in Birmingham and Erlangen. In Amsterdam, an ASUS laptop was used (15.6 inch screen). All laptops operated on Windows 7, 64-Bit. Psychophysics Toolbox Version 3 (*25*) was used with MATLAB 2014 or MATLAB 2009b (Amsterdam). For responses, the following buttons were used: up-down-left-right arrows to select the images during the recall phase, and the 'End' key on the Numpad was used to confirm the selection. During encoding the 'up' and 'down' arrow keys were used to give the plausible/implausible ratings, respectively. During the distractor phase the 'left' and 'right' arrow keys were used to give the odd/even judgements, respectively.

Electrophysiological data were recorded from Behnke-Fried hybrid micro-macro electrodes (Ad-Tech Medical Instrument Corporation, Oak Creek, WI). Each Behnke-Fried hybrid electrode contained 8 platinum-iridium high impedance microwires with a diameter of 38 μm, and one low impedance microwire with the same diameter extending from the tip. Different referencing schemes were used across the hospitals/patients in order to yield the best signal-to-noise ratio in the different environments (i.e. yield highest number of visible spikes in raw data). For 5 patients the high-impedance contacts were referenced against either a low-impedance microwire or macro-contact, thus yielding a more global signal. For the remaining 4 patients high-impedance contacts were referenced against another "silent" (i.e. containing no visually detectable spikes) high impedance wire, thus yielding a more local signal. As part of the pre-processing data were re-referenced to yield a comparable local referencing scheme across all datasets (see below). The data were recorded continuously throughout the experiment on an ATLAS Neurophysiology system (Neuralynx Inc.) with a sampling rate of 32 kHz (Birmingham and Amsterdam) or 32.768 kHz (Erlangen) and stored as a raw signal for processing and analysis.

Data Analysis

<u>Behaviour:</u> Neural activity during the encoding phase was separated into hits and misses according to memory performance in the subsequent recall phase. Hits constitute trials where both items were later correctly retrieved (i.e. complete memory); Misses constitute trials where at least one item was remembered incorrectly or where the patient indicated that they did not remember any item (i.e. incomplete memories or fully forgotten). Reaction times of the plausibility ratings indicate the time from onset of the cue (i.e. animal image) to the button press and were calculated per subject by using the median across trials. Reaction times were 15.01 seconds on average (s.d. 5.79) for hits and 15.26 seconds misses (s.d. 6.85) and did not differ significantly ($t8=0.44$; $p>0.5$).

<u>Electrode localization:</u> Electrodes were localized for using one of the following procedures. For patients recorded in Birmingham and Erlangen, pre- and post-implantation T1 structural MRIs (MP-Rage) were co-registered and normalized to MNI space using SPM8 (https://www.fil.ion.ucl.ac.uk/spm/software/spm8/). If both scans were available the normalization parameters were estimated on the pre-implantation MRI, and these parameters

were then applied on the post-implantation MRI. For two patients, only the post implantation MRI was available. For these two patients normalization parameters were estimated and applied to this post implantation MRI. The location of the microwire bundle was either clearly visible as an image artifact in the post implantation MRI. If not, then the location of the microwire bundle was inferred visually by extrapolating the electrode trajectory by 5 millimetres.
For patients recorded in Amsterdam pre-implantation structural T1 scans and post-implantation CT scans were available. These were overlaid and normalized using the same procedure as described above using SPM8. The microwire contacts were clearly visible in the CT scans, therefore the location could be estimated directly in all cases.

Spike Sorting: Spikes of recorded neurons were extracted offline from high-frequency activity (500Hz-5kHz). Spike detection and sorting was done using Wave_clus(*26*). No attempt was made at isolating single units, and all clusters with at least 50 spikes in either condition (hits, misses), a mean spike count > 2 and mean firing rate > 1 Hz during the encoding period (0-4s) were considered as multiunit activity (MUA). These resulting units were further visually inspected to reject noise based on waveshape, spike distribution across trials, and inter-spike intervals. Across all patients and sessions 218 units were retained for analysis.

Firing Rate and Spike Density: Time stamps of spikes during the encoding phase were extracted and converted to continuous time series containing 0s (no spike) and 1s (spike) at a sampling rate of 1kHz. These time series were cut into trials with a duration of 14 seconds centred to cue onset (i.e. animal image), starting at -7 seconds. These trial-based spike time series were then convolved with a gaussian window of 250 ms length to yield spike density time series per trial. These trial-based time series were averaged separately for hits and misses. Finally, a normalization procedure according to (*27*) was carried out to account for the vast variability of firing rates between neurons (some neurons fire very sparsely whereas other fire at a very high rate). Normalized firing density was calculated according to the formula below, where z (t) = normalized firing rate, sd(t) = spike density, μ(bl)= mean spike density in baseline interval, σ(bl) = standard deviation of spike density in baseline interval, and λ = regularization parameter (set to 0.1; see (*27*)). This regularization parameter was necessary to avoid extreme values for cases where no or only few spikes were present in the baseline. The baseline interval was set to -1000 ms to -125 ms (i.e. half of the Gaussian window length).

$$z(t) = \frac{sd(t) - \mu(bl)}{\sigma(bl) + \lambda}$$

LFP pre-processing: The continuous raw data was imported using the Neuralynx data reader provided by U. Rutishauser (7th release, https://www.urut.ch/new/serendipity/index.php?/pages/nlxtomatlab.html). A Butterworth low-pass filter was applied (filter order 2) at 300 Hz. In some channels/sessions an artifact from the TTL pulse was visible, which was removed by subtracting the average artefact from the single trial using a linear regression. Spikes were removed by linearly interpolating the signal from 2 ms before the spike to 6 ms after the spike (*28*). Line noise at 50 Hz was removed using a template subtraction method. This method estimates the line noise signal by fitting a sinusoid at noise frequency and then subtracting it from the signal. Because the line noise can be assumed to be stationary (whereas brain signals are not stationary) this approach effectively removes line

noise whilst retaining physiological activity. This approach is therefore preferable to a band-stop filter, which does not retain physiological activity at line noise frequency. Finally, the continuous LFP data was segmented into epochs of 14 seconds duration centred at cue onset during encoding (i.e. animal image), downsampled to 1 khz using Fieldtrip (*29*), and stored for further analysis.

The LFP data was cleaned from artefacts and re-referenced as follows. For artefact rejection a two-step procedure was carried out which first identified noisy channels, and then noisy trials. To reject noisy channels the root mean square amplitude (RMSA) in the time window of interest (-0.5 to 5 seconds around cue onset) was calculated for each channel and z-transformed (where the mean and standard deviation were obtained across channels). Channels with a z-value above 3 were rejected. On the trial level, a similar procedure was carried out on those channels retained after the first step. The RMSA was averaged in the time window of interest (-0.5 to 5 seconds) and z-transformed across trials. Trials with a z-value of over 4 were rejected. Furthermore, z-scores were calculated for the raw amplitude. Trials with a maximum raw amplitude z-score of above 4 were also rejected. Lastly, only channels with a minimum of 25 remaining trials were submitted to further analysis.

Finally, the data were re-referenced to yield a comparable signal across patients and to extract the field potential on a very local level. To this end each microwire channel was re-referenced to the mean amplitude of its neighbouring microwire channels (i.e. wires on the same bundle). Bundle refers to the 8 high-impedance contacts within one Behnke-Fried hybrid electrode. Instead of simply subtracting the average signal, however, we used an orthonormalization procedure termed Gram-Schmidt Correction (see https://en.wikipedia.org/wiki/Gram–Schmidt_process). This procedure projects two signals into a sub-space where both signals don't share any variance, i.e. they are orthonormal to each other (their sum = 0). This is an effective way of subtracting those parts of a signal, which are shared between an individual channel and its neighbours (such as volume conduction; see (*30*)). Furthermore, by only subtracting those parts of the signal that are shared between the two sources this method is less prone to introducing noise from the reference into the referenced channel.

<u>Spike Field Coupling:</u> The following procedure was used to calculate spike field coupling (SFC) and to assess differences in SFC between hits and misses. As an overview, this procedure calculated spike field couplings for every possible pairing of units (spikes) and LFP channel. Therefore, a given pairing could either constitute coupling at the local level (i.e. spike and LFP come from the same channel, or from the same bundle), or coupling at a distal level (i.e. spike and LFP come from different bundles; see Figure 2 and 3). Each pair was first tested for significant spike field coupling and then submitted to further analysis to compare SFC between hits and misses.

As a first step, phase was calculated using fieldtrip. Different parameters were used for low (2-40 Hz) and high frequency ranges (40-80 Hz); i.e. using a 6 cycle wavelet for low frequencies in steps of 1 Hz and a 12 cycle wavelet for high frequencies in steps of 2 Hz. In addition, for high frequencies only the first derivative was taken before calculating phase. Phases at spike times were extracted and split according to whether they occurred the time window of interest, which was 1 second after the face/place stimuli were shown (2 – 3 seconds after Cue onset). If at least 30 spikes were available then the data was admitted to the next step. For a given spike-LFP pair a Raleigh test using the Circ_Stat Toolbox (http://www.jstatsoft.org/v31/i10) was calculated at each frequency to assess whether phase distributions were different from a uniform distribution.

An FDR correction (*31*) was applied to correct for multiple comparisons across frequencies. If this corrected p-value was below 0.05 then the spike-LFP pair was submitted to the next step. In this step, pairwise phase consistency was calculated for three conditions, (i) across all trials (hits and misses together), (ii) only for hits (i.e. later completely remembered trials), and (iii) only for misses (i.e. partially remembered and fully forgotten trials).

To statistically assess whether the number of significant spike – LFP couplings identified in the above procedure was above chance a randomization test was carried out. This test was run separately for locally coupled and distally coupled spike – LFP pairs. To this end, trials for the spike providing data and phase (i.e. LFP) providing data were shuffled. All other parameters (including number of hit and miss trials) were held constant. These shuffled data were then subjected to the same Raleigh test (FDR corrected) as above. For each possible spike-LFP pair 100 such shuffled tests were carried out and the data was stored. From these shuffled data a distribution of the number of 'significant' spike-LFP pairs (i.e. Raleigh test $p < 0.05$; FDR corrected) was generated by drawing 10000 samples, counting the number of significant spike-LFP pairs for each sample.

To extract the peak frequency of spike field coupling a peak detection on the individual PPC spectra was run using the findpeaks command in Matlab. For theta the PPC spectrum was restricted to a frequency range between 3 to 13 Hz, and for gamma between 45 to 75 Hz. The peak PPC had to surpass a threshold of 0.005 for both hits and misses, to ensure that meaningful PPC was present in both conditions.

<u>Non-stationarities of LFP:</u> One may be concerned about non-stationarities of the signal and whether such non-stationarities affect the phase estimations obtained with the here applied Wavelet analysis. A specific concern is that the phase obtained from the Wavelet analysis is not correct when the instantaneous frequency of the LFP signal does not match the frequency of the Wavelet. This concern was addressed in two ways.

In a first step, a simulation was carried out where an oscillator in the LFP signal transitions randomly between frequencies with a mean frequency of 6 Hz fluctuating between 3.5 to 9 Hz, thus exhibiting strong non-stationaries across a wide range. Spikes of a hypothetical neuron were simulated to be locked to the trough of this non-stationary oscillator (see Fig S5A-B). White noise was added to the simulated signal. The results of this simulation demonstrate that the mean frequency of spike phase locking at 6 Hz is correctly retrieved by the Wavelet analysis (Figure S5C). Crucially, the mean phase of spiking is also correctly retrieved (Figure S5D). The same simulation has been carried out for the high-frequency range with similar results. From this we can conclude that our Wavelet based approach is well suited to recover the mean frequency and mean phase of coupling between a spiking neuron and a non-stationary oscillator.

In a second step, we repeated the spike-LFP coupling analysis using a combination of band-pass filter and Hilbert transformation. The band-pass filter (Butterworth) was set to a width of 4 Hz for the low frequency range, and 8 Hz for the high frequency range, thus leaving ample opportunity for variations in instantaneous frequency. Trials were segmented as before to 14 seconds centred at the onset of the cue stimulus (i.e. animal), to ensure that filter artifacts at the beginning and end of the trial are well out of the time window of interest (i.e. 2-3 seconds after cue onset). The band-pass filter was implemented using the ft_preprocessing command in fieldtrip centred at discrete steps of 1 Hz between 3 to 40 Hz (i.e. 3 = 1 to 5 Hz; 4 = 2 to 6 Hz; … 40 = 38 to 42 Hz) and 2 Hz between 40 to 80 Hz (i.e. 40 = 36 to 44 Hz; 42 = 38 to 46 Hz; … 80 = 76 to 84 Hz). Phase was estimated using the Hilbert transform as implemented in fieldtrip

(ft_preprocessing) and phase variance was obtained using pair-wise phase consistency (PPC) as described above. The results of this analysis are reported in Supplementary Figure S6.

Directionality of distal theta spike-field coupling: To assess the direction of information between spikes and distally coupled LFPs the Phase Slope Index (PSI) was applied (*32*). The PSI is a frequency resolved measure of the direction of information flow between two time series A and B. As most directional coupling measures, the phase slope index assumes that it requires time for a signal to travel from A to B. If the speed at which different waves travel is similar, then the phase difference between sender and recipient increases with frequency and we expect a positive slope of the phase spectrum. Hence, a positive phase slope indicates that A is the sender and B is the receiver, and vice versa. We preferred the phase slope index over Granger causality as it requires less assumptions and is less sensitive to noise (*32*). The PSI was calculated using the ft_connectivityanalysis function in fieldtrip using a bandwidth of 5 Hz (i.e. phase slopes are estimated over a 5 Hz window). Spike time series were convolved with a Gaussian window (25 ms) to yield a continuous spike density signal. The raw PSI values were baseline corrected using a z-transformation to ensure an unbiased comparison between hits and misses. To this end, trials for the spike providing signal were shuffled 100 times and submitted to the same PSI analysis as the real data. This shuffling was carried out separately for hits and misses, thereby keeping the number of overall spikes constant. The mean and standard deviation across shuffles was calculated and used for z-transformation of the PSI values of the real (i.e. un-shuffled) data. Finally, a minimum of 60 spikes was imposed to allow for a meaningful analysis of directional information flow between the two signals.

SFC control analysis for selection bias: In the above analysis only spike-LFP pairs, which show significant phase coupling across all trials are subjected to further analysis. This could introduce a potential bias, especially for cases where firing rates and trials are not evenly distributed between conditions (hits vs. misses). This concern would be especially problematic if the results would show an overall increase in spike-field coupling for hits vs. misses, as opposed to differences in peak frequencies as shown here. Nevertheless, we accounted for this issue by means of a control analysis. In this control analysis, PPC values for a given spike-LFP pair were calculated for 5000 instances where the trials for spike providing and LFP providing data were shuffled. As above, all other parameters (importantly number of hit and miss trials were kept constant). After each shuffle a Raleigh test as above was carried across all trials. If this test retained a p-value <0.05 (FDR-corrected) PPC spectra were calculated for ‘pseudo-hits’ and ‘pseudo-misses’. These spectra therefore contain the same selection bias as in the real analysis because the ratio between hits and misses has been kept constant, and therefore provide a baseline for hits and misses which can be used to effectively correct for this bias. Accordingly, PPC values for each spike-LFP pair for the real data were z-transformed using this baseline by subtracting the mean across ‘significant’ shuffle runs and dividing by the standard deviation. This bias corrected data was submitted the same peak detection analysis as the real data and similar results were obtained (see Figure S4).

Theta-Gamma Interaction: In order to assess the spatial overlap of local SFC in the gamma range and distal SFC in the low frequency range the number of spike-LFP pairs were counted that exhibited both phenomena in the same region (i.e. same microwire bundle). Cross-frequency coupling (CFC) was then analysed for these overlapping pairs of locally and distally coupled

spike-LFP channels. To this end, both theta and gamma LFPs were taken from the same bundle of microwires and therefore were recorded in the same region (or at least in very close proximity; see Figure 4A-B). The PAC analysis therefore does reflect the temporal coordination of theta and gamma oscillations in a local region. It is only that the locally recorded theta is phase locked to a spike recorded in another, distally coupled, region. For each channel pair the peak gamma frequency, and the peak theta frequency was extracted from the PPC spectra. Importantly, these peaks were extracted separately for hits and misses, to account for the difference in frequency between the two conditions. Peaks at gamma were restricted to a frequency range between 50 to 80 Hz, and 5 to 11 Hz for theta. Phase for the lower frequencies (i.e. theta) and power for the higher frequencies (i.e. gamma) were calculated using the same wavelet parameters as above (i.e. 6 cycles for theta, 12 cycles for gamma). Cross-frequency coupling was then calculated via the Modulation Index (*23*) using the function 'ModIndex_v2.m' provided by Adriano Tort with a binning parameter of 18 bins (https://github.com/cineguerrilha/Neurodynamics/blob/master/16ch/Comodulation/ModIndex_v2.m). The MI was calculated separately for hits and misses. Because the MI is affected by trial numbers, a normalization procedure was applied to yield a bias free CFC measure for hits and misses. To this end, trials for the phase providing channel were shuffled and MI was calculated after each shuffle (N=200). This was done separately for each condition (hits and misses) to generate a baseline MI under the null for each condition. The mean and standard deviation across the shuffled data was then used to z-transform the MI of the real data.

Power Analysis: Power of LFP data was calculated using the same wavelet parameters for high and low frequency ranges as above. Raw power values were z-transformed for each channel separately using a common procedure for analysing subsequent memory effects (*15, 33, 34*). Power values for each channel, frequency band and trial, were first averaged across time (-0.5 to 5 seconds). Then the median and standard deviation of this time-averaged power across trials was calculated. Power values for each channel, frequency bin and trial were then z-transformed by subtracting median power and dividing by standard deviation. Trials containing outlier power values (i.e. maxima > 2.5 of standard deviation of maxima across trials) were discarded. Finally, trials were split according to conditions (hits and misses) and averaged. Power for low frequencies was calculated for channels which showed a significant SFC in the low frequency range, whereas power for high frequencies was calculated only for those channels showing significant SFC in the high frequencies.
An additional power analysis was carried out to assess the presence of a meaningful signal at the frequencies where spike-LFP coupling was observed. To this end power at spike times was extracted for distally coupled LFPs in the low frequency range, and locally coupled LFPs in the gamma frequency range using the same Wavelet filter as used for SFC analysis. Power spectra were 1/f corrected by fitting and subtracting a linear function to the log-log transformed power spectra. The resulting spectra were then back transformed to linear space and centred at the peak frequency of PPC. Lastly, power values were normalized for each LFP channel by subtracting the mean across the whole spectrum and dividing by the standard deviation across the whole spectrum.

Inter-trial Phase Consistency: Inter-trial phase consistency was calculated for the lower frequency range (i.e. 2 – 40 Hz) using pairwise phase consistency (PPC)(*20*). Phase for each single trial was extracted using the same wavelet transformation (6 cycles) as above. PPC spectra

were limited to a frequency range of interest (2-13 Hz), comprising the slow and fast theta range. PPC spectra were calculated for hits and misses separately and only for those channels showing significant SFC in the low frequency ranges.

Spike Power Analysis: To test for the presence of theta rhythmicity within the spiking of neurons an FFT analysis was carried out on the spike density time series. Spike time series were convolved with a Gaussian window (25 ms) to yield a continuous spike density signal for the time window of interest (2-3 seconds after cue onset). These trials where then submitted to a FFT analysis using the ft_freqanalysis command in fieldtrip, with a Hanning taper and frequency smoothing of +/- 2 Hz.

Theta Waveshape Asymmetry: To assess the presence of asymmetric theta waveforms, which could give rise to spurious cross-frequency coupling at harmonics of theta, two control analyses were performed. For the first control analysis, MIs were calculated exactly the same way as for the real data, except that for each LFP signal the gamma frequency was taken as the 8th harmonic of the theta in that signal (i.e. for theta = 9 Hz, gamma = 9 * 8 = 72 Hz). We took the 8th harmonic as this was the frequency that was on average closest to the observed gamma frequency (i.e., 64 – 72 Hz). The 8th harmonic was estimated based on the dominant theta frequency separately for hits and misses. Next, we calculated the difference in MI between hits and misses. If asymmetric theta gives rise to the difference in CFC the real data then this effect should even be stronger in the control data where gamma was centred at the harmonic of theta. However, we observed the opposite pattern, with the real data showing stronger differences between hits and misses compared to the harmonic control data (Figure S5A).
In a second control analysis, the asymmetry index was calculated following the procedure described in (*35*). To this end, the LFP data for hits and misses was filtered at the theta phase providing frequency band +/- 2 Hz used for CFC analysis, using a Butterworth bandpass filter implemented in Fieldtrip. Then the filtered data was cut to the time window of interest (2-3 seconds) and peaks and troughs were identified using the 'findpeaks' function in Matlab. Thereafter, peaks and troughs of the filtered data were adjusted by matching them with peaks and troughs in the unfiltered data. This matching process searched for local maxima and minima in a time window of a quarter cycle length of the theta frequency (i.e., 5 Hz = 200/4 = 50 ms) centred at the peak located in the filtered data. The time stamps of these adjusted peaks and troughs were then used to calculate the asymmetry of the theta waveshape using the formula below. Where *Tasc* is the duration of the ascending flank, *Tdesc* is the duration of the descending flank, and ω is the cycle length of the theta frequency. *Tasc* was calculated by subtracting the time stamp of the trough from its subsequent peak (i.e. T peak(t+1) – T trough(t)); Tdesc was calculated by subtracting the time stamp of the peak from its subsequent trough (i.e. T trough(t+1) – T peak(t)). Therefore, both Tasc and Tdesc always yield positive values. The asymmetry index (AI) is a normalized measure ranging between -1 and 1 with negative values indicating longer durations of descending flanks, and positive values indicating longer durations for ascending flanks.

$$AI = \frac{Tasc - Tdesc}{\omega}$$

To verify that this index detects the presence of asymmetric waveforms a dataset recorded in the rodent entorhinal cortex was used as a positive control (courtesy of Ehren Newman). The data comprised 10 minutes of open field navigation of the rodent. Clear ongoing theta activity was present in this data and indeed a strong asymmetry could be detected (Figure S5B). For the human data, AIs were averaged across trials for hits and misses separately to yield one AI per channel. AIs between hits and misses were compared using a paired samples t-test. No difference in asymmetry between hits and misses was obtained (see Figure S9C), which further rules out an influence of asymmetric waveshapes on the observed cross-frequency coupling results.

Co-firing Analysis: Co-firings between pairs of neurons at different time lags were calculated via cross-correlations using the xcorr function in Matlab. To this end, spike time series for each unit were concatenated across trials to yield one vector and convolved with a Gaussian envelope with a width of 25ms (~10ms full width half maximum). Cross-correlations were calculated for pairs of putative 'sending' units, and putative 'receiving' units. Putative sending units were units, which showed a significant distal SFC in the low frequency range, and where the distally coupled LFP was in addition locally coupled to a unit in the high frequency (gamma) range. This locally gamma coupled unit was taken as the putative receiving unit. Accordingly, the pairs were chosen such that the region were the sending unit was coupled to is the same as the region where the local coupling occurs. This resulted in a relatively low number of neural pairs (N=24), because two conditions needed to be met. More specifically, for a pair of neurons to be considered as such the putative sending neuron needed to show significant distal low frequency coupling to the region where the putative receiving neuron was located; additionally, the receiving neuron needed to be significantly coupled to local gamma oscillations. This selection and labelling of units into sending and receiving units is supported by the directional coupling analysis (see Fig 4). Altogether, 5 patients contributed data to this analysis, with a median of 5 pairs per patient, and a minimum and maximum of 2 and 8 pairs per patient, respectively (see Supplementary Table S1). Cross-correlations between putative sending and putative receiving units were calculated separately for hits and misses. To correct for a potential bias of numbers of spikes, cross-correlation values for hits and misses were z-transformed according to a shuffled baseline. To this end, trials for the putative receiving unit were shuffled 2000 times and submitted to the same cross-correlation analysis as the real data. This shuffling was carried out separately for hits and misses, thereby keeping the number of overall spikes constant. The mean and standard deviation across shuffles was calculated and used for z-transformation of the cross-correlation values of the real (i.e. un-shuffled data). As a final step, only cross-correlations for pairs of neurons where the average co-incidence (mean across hits and misses) exceeded 1 at any lag were admitted to statistical analysis. This step ensured that only pairs of neurons with meaningful co-firings were used. To compare the latencies of co-firing between hits and misses a peak detection was carried out using the findpeaks function in Matlab.

Spike Phase Analysis: Phases at spike times were extracted for neuron pairs of putative sending and putative receiving neurons as defined in Co-firing Analysis (see above). This analysis was done to test whether the differences in co-firing lags could be explained by differences in phase of firing. To this end, the phase of the LFP at the time of firing was extracted for distally coupled theta and locally coupled gamma spike-LFP pairs. For distally coupled theta pairs, the LFP at the putative receiving region was extracted and submitted to a Wavelet analysis (same parameters as for the Spike Field Coupling analysis). For locally coupled gamma pairs, the locally coupled LFP

at the putative receiving region was extracted. Phases were extracted separately for spikes that occurred during hit trials and miss trials in the time window of interest (2-3 seconds). Phase angles were extracted at the peak theta and peak gamma PPC frequencies as calculated previously (see Spike Field Coupling) and averaged to get a mean phase direction for hits and misses per spike-LFP pair. Finally, the difference phase angle (hits – misses) was calculated for each spike-LFP pair and tested for deviation from uniformity using a Raleigh test. Results of this analysis are shown in Fig. S11.

Computational Modelling: The model consisted of two groups of neurons, one to represent distal hippocampal neurons (Ndis = 100) and one to represent local hippocampal neurons (Nloc = 100). Neurons were simulated using the leaky-integrate-and-fire equation (Equation 1), where a real biological neuron is assumed to exist as an abstract single point in space, represented by a singular membrane potential (Vm).

$$C_m \frac{dV_m}{dt} = g_m(E_L - V_m) + I_{syn} + I_{AC}$$

Equation 1 – Update equation for the leaky-integrate-and-fire neuron, using the Euler method to integrate with a time-step of 1 millisecond.

For each simulated neuron, a membrane potential (Vm) is updated through time, which gravitates towards a resting potential (EL = -70mV) at a particular rate dictated by neuronal conductance (gm = 0.03mS). Alternating current is injected into model neurons (IAC) to represent input from network oscillatory activity, whilst a synaptic current (Isyn) represents input from dendritic connections. Both inputs are moderated by the total membrane capacitance of the neuron (Cm = 0.9F/cm2). A spike event occurs when the membrane potential reaches a threshold (Vth = -55mV), at which time the membrane potential is reset to the resting potential for an absolute refractory period (Vref = 2ms) and a spike event is sent to downstream neurons after a delay (D = 2ms).

$$\alpha(PSP) = w \cdot \rho(t) \cdot \left(e \cdot \frac{t}{\tau_s}\right) \cdot e^{-\frac{t}{\tau_s}}$$

Equation 2 – Exponential alpha function for a post-synaptic potential (PSP).

Spike events trigger a post-synaptic potential (PSP) in receiving neurons (Equation 2), whereby a time constant (τs) dictates the length of time it takes for voltage increments to decay to 2/3 of the maximum value. The amplitude of the PSP is calculated as the value of the synapse ($0 \leq \rho \leq 1$) multiplied by a weight value. All neurons received noise that randomly fluctuated the membrane potentials. This was in the form of a Poisson distribution of spike events at a rate of 4000 spikes per second (τs = 15ms) with weights of 0.00175mS/cm2 for distal neurons, and a rate of 1000 spikes per second (τs = 1.5ms) with weights of 0.08mS/cm2 for local neurons.

$$F_{LTP}(t,i) = \sum_{t_i<t}^{n_{pre}} A_+ \cdot e^{\frac{t_i - t}{\tau_s}}$$

$$F_{LTD}(t,j) = \sum_{t_j<t}^{n_{post}} A_- \cdot e^{\frac{t_j - t}{\tau_s}}$$

Equations 3.1 - 3.2 – Synaptic plasticity functions (FLTP & FLTD) calculate potential plasticity as the summation of the total number (npost & npre) of historic spike events (ti & tj) arriving at a post- (i) or pre-synaptic (j) synapse relative to the time of a given spike event (t). Plasticity functions are separated for both long-term potentiation (LTP) on post-synaptic connections & long-term depression (LTD) on pre-synaptic connections.

$$\forall i. \frac{d\rho(i)}{dt} = \gamma_p\big(1 - \rho(i)\big) \cdot H[F_{LTP}(t,i) - \varepsilon_{LTP}] \cdot [F_{LTP}(t,i) - \varepsilon_{LTP}]$$

$$\forall j. \frac{d\rho(j)}{dt} = -\gamma_d \cdot \ \rho(j) \cdot H[F_{LTD}(t,j) - \varepsilon_{LTD}] \cdot [F_{LTD}(t,j) - \varepsilon_{LTD}]$$

Equations 4.1 – 4.2 – Actual plasticity acting on a synapse ($0 \leq \rho \leq 1$) at the occurrence of a spike event (t). Post- (i) & pre-synaptic (j) efficacy changes are induced by potential plasticity functions (FLTP & FLTD, respectively) being above a threshold (εLTP & εLTD, respectively). The sets i & j represent the indices of all post- & pre-synaptic synapses of the spiking neuron, respectively.

When spikes occurred at both a pre-synaptic & a post-synaptic neuron, spike-timing-dependent-plasticity (STDP) could potentiate or depress the synaptic connection (Equations 3-4), dependent on the order of spiking (Markram et al., 1997). Here, we adapt a classic STDP model (Song et al., 2000) by applying a threshold mechanism, similar to more recent calcium dependent models (Graupner & Brunel, 2012). This adaptation was undertaken to encourage the link between higher frequency bursting and synaptic plasticity, as is indicated by findings from a hippocampal culture study (Huerta & Lisman, 1995).

Equation 3.1 details how potential long-term potentiation (LTP) at the post-synaptic connection (i) was calculated as the summation of historic pre-synaptic spikes (npre) that occurred before an eliciting spike event at time t (where ti < t), weighted by an absolute value (A+ = 5 for distal-to-local synapses & A+ = 1 for local-to-local synapses). Contributions of pre-synaptic spikes were proportional to an exponential decay, thus favouring spikes that occurred close together in time (τs = 25ms). Similarly, Equation 3.2 details how potential long-term depression (LTD) at the pre-synaptic connection (j) was calculated as the summation of historic post-synaptic spikes (npost) that occurred before an eliciting spike event at time t (where tj < t), weighted by an absolute value (where A- = 1.1·A+ to promote network stability, Song et al., 2000).

Equations 4.1-4.2 describe how potential plasticity was converted to actual plasticity at the time of the eliciting spike (t). Here, synapses changed in proportion to their prior values such that $0 \leq \rho \leq 1$. Synaptic change was modulated by an absolute rate (γp = 1 for LTP & γp = 0.5 for LTD), relative to how much potential plasticity was above a threshold. This is captured by use of a

Heaviside function (H[]), which returns a binary 1 or 0 dependent if potential plasticity (FLTP or FLTD) was above a plasticity threshold (where εLTP & εLTD = 0.5). The degree of plasticity is then dictated by the difference between potential plasticity and the respective threshold, causing an exponentially graded plasticity effect that favours cellular bursting for the induction of plasticity on a synapse (Huerta & Lisman, 1995).

There was no interconnectivity within the distal group, as it was assumed that distal neurons were a set of independent contributors to each local neuron, which were themselves being independently observed. A set of connections was set up both within the local group and from the distal group to the local group, both with 10% random sparse connections with a new random seed for each initialisation (where τs = 20ms for distal-to-local synapses & τs = 1.5ms for local-to-local synapses, w=0.1mS/cm2 for all synapses). These synapses were initialised such that ρ=0.05, able to rise up to ρ=1 through STDP.

The aim of the model was to determine whether faster frequency oscillations are more conducive towards STDP. As such, two parameter settings were established for successful & unsuccessful simulations (i.e., "hits" & "misses"). The distal neuronal group received a cosine alternating current (IAC) to simulate a θ-rhythm (for "hits:" frequency = 9Hz; for "misses:" frequency = 5Hz), as we have shown that a fast θ-rhythm is correlated to successful memory encoding (see Figure 3). The amplitude of the simulated θ-rhythms varied with respect to θ-frequency to account for a decrease in rise time for higher frequencies, such that a similar amount of spiking was produced for different frequencies (where amplitude = 0.15·exp[f/7]). This enabled a fair comparison between conditions in determining the effect of frequency on network plasticity. To maintain a predictable lag in time between distal and local spikes (see Figure 5), it was essential that the local neuronal group received a phase-reversed θ-rhythm (amplitude = 0.375mA; for "hits:" frequency = 9Hz; for "misses:" frequency = 5Hz). It was assumed here that the θ-rhythm oscillation filtered through distal neurons towards local neurons, causing a phase-reversal upon its arrival. This way, the temporal lag between distal and local spikes is inversely correlated to θ-rhythm frequency, such that higher frequencies reduce the lag between conversing distal and local neurons. This ultimately has the effect of increasing the likelihood of STDP, as Δt between pre- & post-synaptic spikes is reduced for higher frequencies. Further to this more general θ-rhythm input, local neurons also received a more specific coupled θ:γ rhythm (for "hits:" frequency = 9:70Hz; for "misses:" frequency = 5:60Hz), which was assumed to be the driving force of distal-local communication and learning (Equation 5). Similarly, the amplitude of simulated θ:γ rhythm also varied with respect to γ-frequency (where amplitude = 0.4·exp[f/30]).

$$\theta{:}\gamma(t) = \big(\theta(t) \cdot CFC + (1 - CFC)\big) \cdot \gamma(t)$$

Equation 5 – Function to compute θ:γ cross-frequency coupling.

This resultant alternating current (IAC) was calculated as the product between a θ-rhythm ($0 \leq \theta \leq 1$), which was modulated by a cross-frequency coupling factor ($0 \leq CFC \leq 1$), and a γ-rhythm ($-1 \leq \gamma \leq 1$). This was used to determine the degree to which the θ-rhythm drove the local γ-rhythm. Here, a value of 1 produced high θ:γ coupling and a value of 0 returned a γ-rhythm with no θ-modulation at all. Observations presented here indicate that successful trials have a prevalence of θ:γ coupling, whereas unsuccessful trials did not (see Fig. 5). Therefore, in the forthcoming simulations "hits" had a high CFC value of 0.8, whilst "misses" had a low CFC value of 0.1. In all, the total oscillatory input to local neurons can be summarised as the sum of a

general θ-rhythm and a local θ:γ-rhythm for "hits," or the sum of a general θ-rhythm and a local γ-rhythm for "misses." Additional irregularity was added to each simulated trial by varying certain parameters around a normal distribution, such that the stated values for oscillatory amplitude & all neuronal weight values varied on a neuron-by-neuron basis (such that the stated value was multiplied by a normal distribution with mean 1 and standard deviation 0.2). As well as complementing the robustness of the model, this also aided learning within the self-organising plastic network.

Supplementary Text

Firing Rates

During encoding, trials which resulted in a complete memory (hits) showed a sustained increase in firing rates compared to trials resulting in incomplete or no memory (misses; see Figure S1). This "subsequent memory effect" (SME) started approximately 1 second after the onset of the associative stimuli. A two-way repeated measurements ANOVA with the factors Memory (Hits vs Miss) and Time (Cue, Association Stimulus, Response) revealed a significant interaction ($F_{2,434}=7.16$; $p<0.001$). This effect was due to hits showing significantly higher firing rates than misses in the Response period (3-5 seconds; $t_{217}=3.79$; $p<0.0001$). No significant differences were observed during the Cue period (0-2 seconds; $t_{217}=1.89$; $p>0.05$), or during the Association Stimulus onset (2-3 seconds; $t_{217}=0.95$; $p>0.3$). Significant SMEs in the Response period were also obtained in more conservative statistical approaches, where sessions were used as random variable ($t_{35}=2.25$; $p<0.05$).

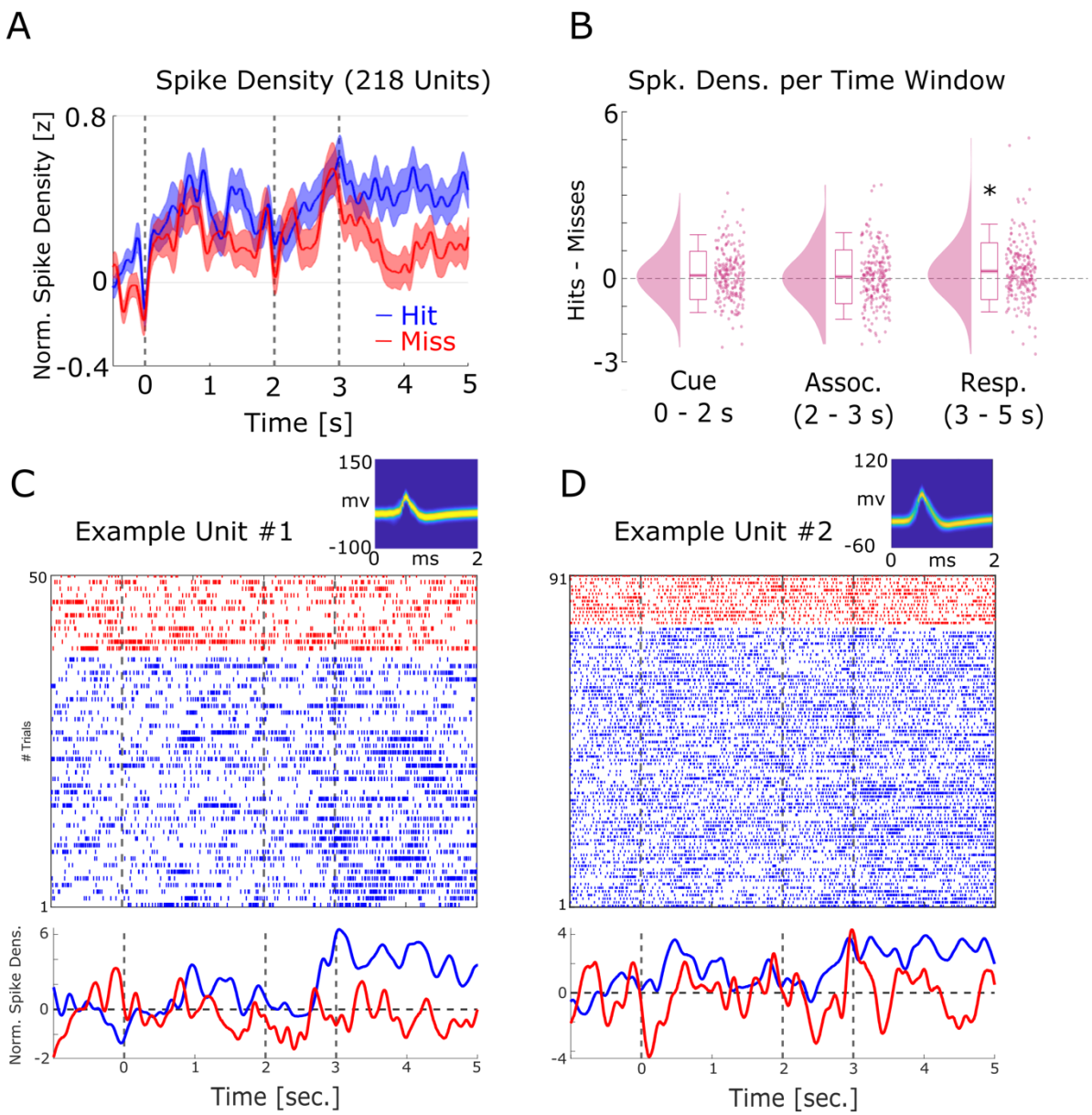

Fig. S1. Firing rate effects during memory encoding.
(A) Averaged normalized population spike densities are plotted for hits and misses. Hits show a sustained increase in firing after 3 seconds compared to misses. Shaded areas indicate standard error of the mean. (B) The difference between hits and misses is shown for the three time windows of interest. A significant increase for hits > misses was only observed for the response time period. (C) and (D) Two example single units are shown. Wave shapes on the top right are plotted by means of 2D histograms (see (*36*)). The plots beneath the raster plots show the normalized spike densities for hits (blue) and misses (red).

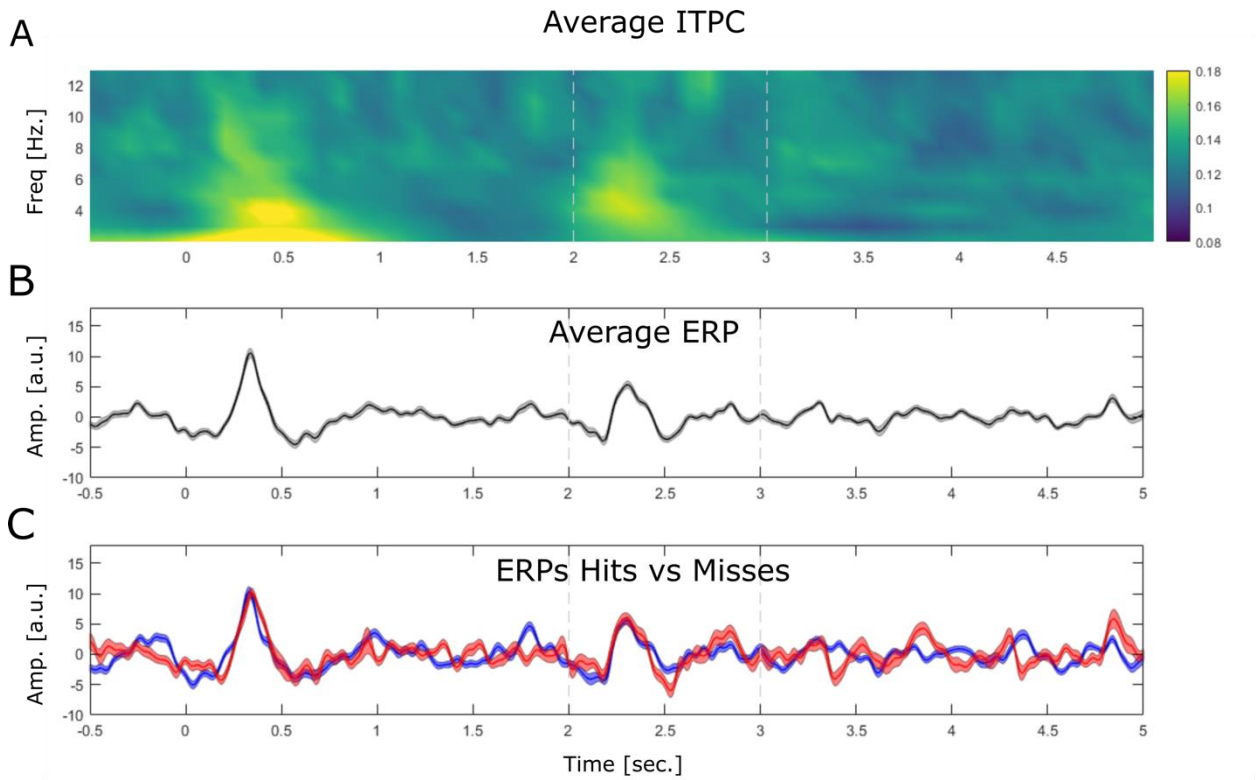

Fig. S2. Stimulus evoked LFP activity is shown by means of inter-trial phase coherence (ITPC) and event related potentials (ERPs).

(A) ITPC is plotted by means of phase locking value (PLV). The data shows a robust evoked response at the onset of the cue stimulus (0 sec.) and the onset of the association stimulus (2 sec.) albeit the latter appears to be slightly weaker. (B) The ERP is shown averaged across all trials, electrodes and sessions. (C) The ERP is shown for hits (blue) and misses (red). Note that no differences between ERP components between hits and misses is observed.

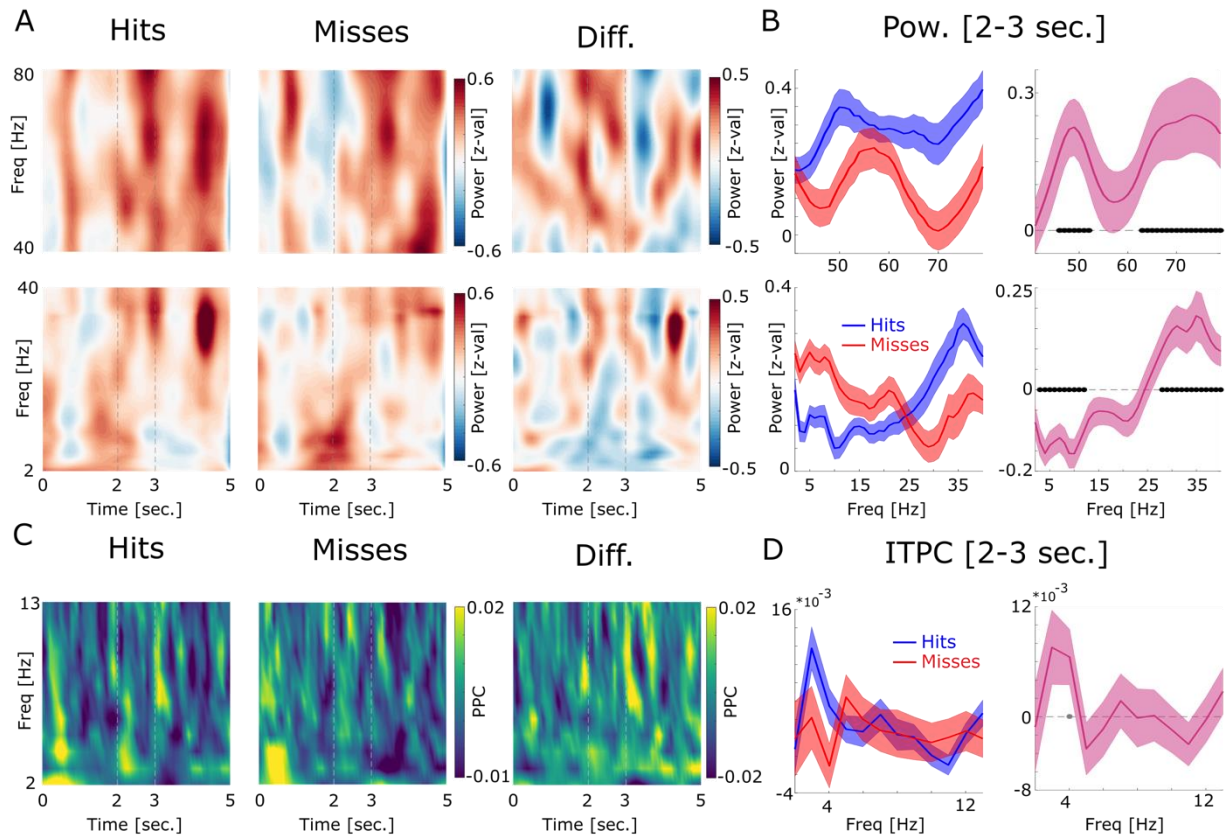

Fig. S3. LFP power and intertrial phase coherence (ITPC) results are shown.
(A) Power for high (top) and low frequencies are plotted for hits, misses and the difference. Time axis indicates time from cue onset. The dashed lines indicate the time window of association period. (B) Power during the association period is shown for hits (blue) and misses (red) and the difference (pink). Low frequencies show decreased power for later remembered associations, whereas high frequencies show increased power for later remembered associations which is a typically observed pattern (*16*). Concerning the higher frequency range, hits show increased power in a slow (45 – 50 Hz) and a fast gamma band (65 – 80 Hz) compared to misses. Filled black circles indicate $p<0.05$, FDR-corrected. (C) ITPC results are shown by means of pairwise phase consistency (PPC) for hits, misses and the difference. Increased phase concentration across trials is observed for the low theta frequency band at the onset of the cue stimulus, as would be expected, and somewhat weaker at the onset of the association stimulus (cf. Fig. S2). (D) PPC results are shown for the association time window (2-3 sec.) for hits, misses and the difference. No significant difference between hits and misses was observed, albeit hits showed a trend for increased phase coherence at 4 Hz compared to misses ($p<0.05$; uncorrected; grey filled circle).

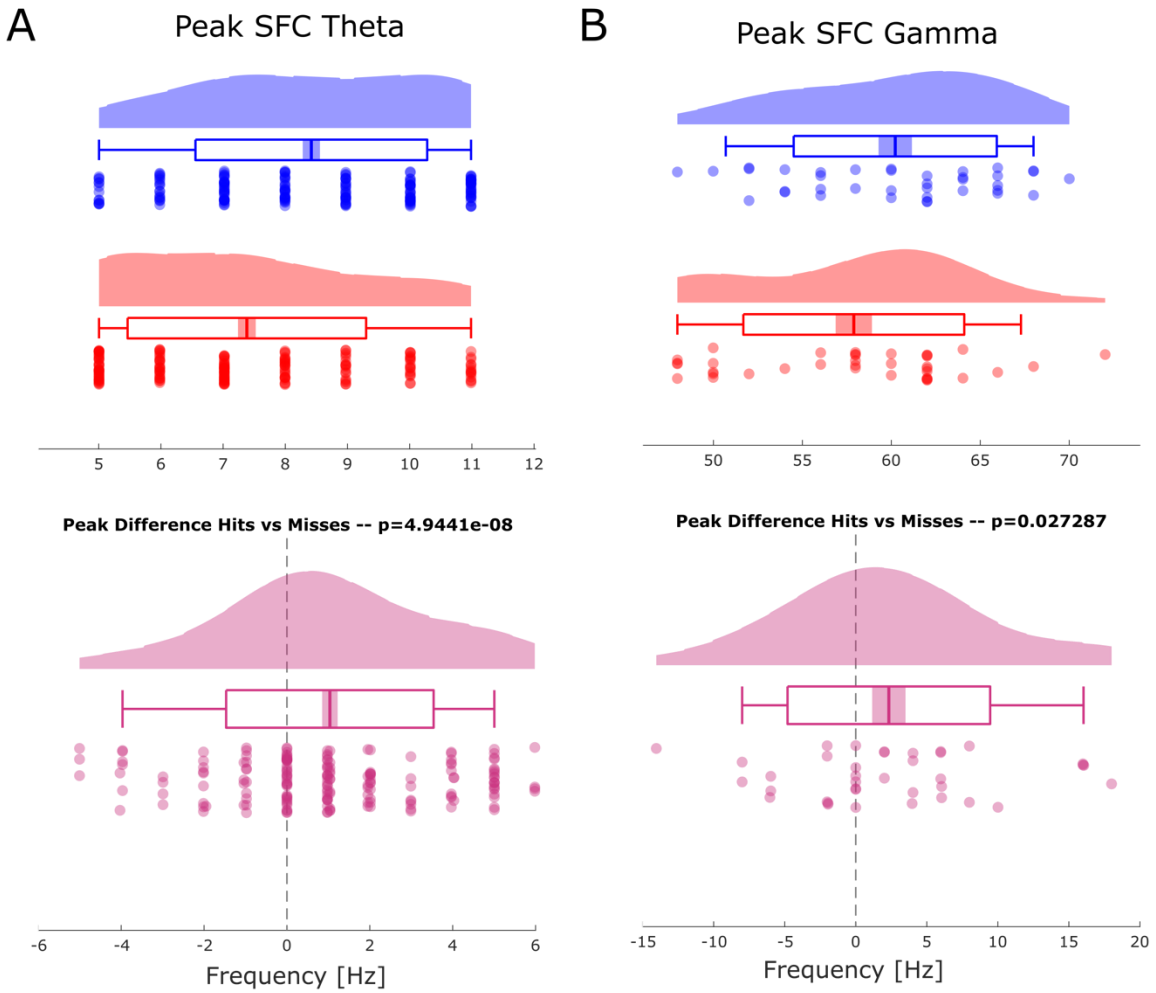

Fig. S4. Selection bias control analysis

Results of a control analysis are shown to rule out a possible bias on the Spike-Field Coupling results due to unbalanced trial numbers. Both control analysis replicated the original results showing faster theta frequencies for hits (blue) compared to misses (red, compare Figure 3 in main text), and faster gamma frequencies for hits compared to misses (compare Figure 2 in main text). (A) The results of the control analysis are shown for theta. (B) The results of the control analysis are shown for gamma.

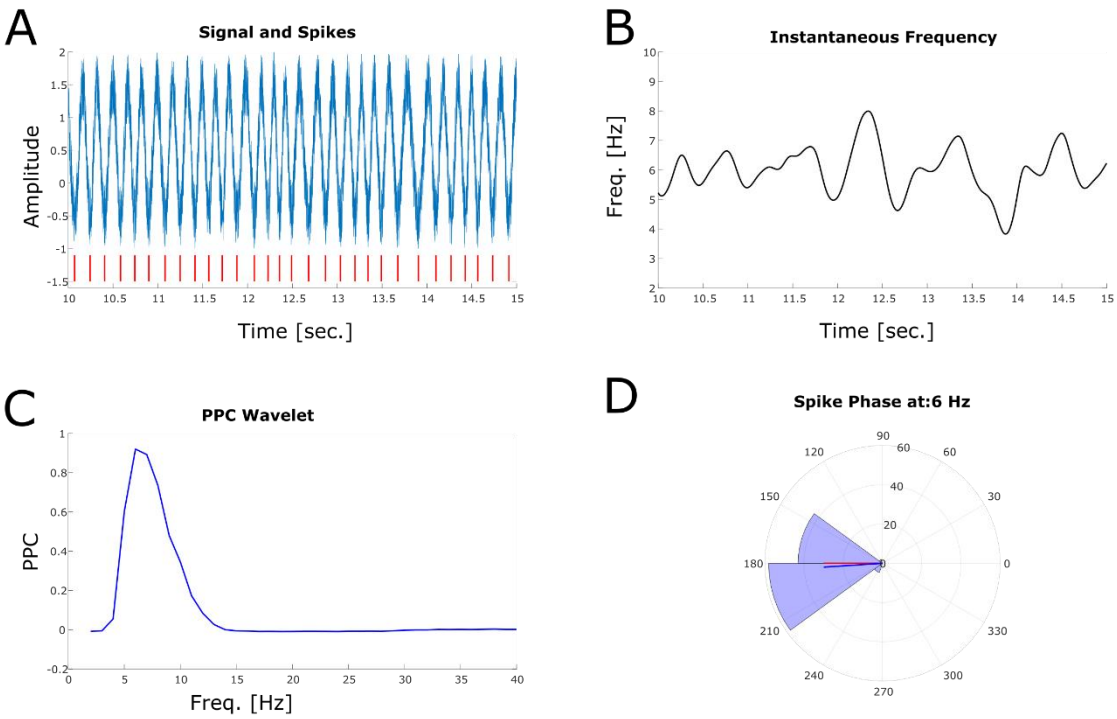

Fig. S5. Simulation of the effects of a non-stationary oscillator on Wavelet analysis. A) A signal is simulated that randomaly transitions between slower and faster frequencies with a mean frequency of 6 Hz (range: 3.5 – 9 Hz). White noise is added to the signal. Spikes are shown on the bottom (red ticks). Spikes are locked to the trough. An epoch of 42 seconds has been simulated but here only 5 seconds are shown. B) Instantaneous frequency is plotted (derived from the simulated signal before adding noise using 'instfreq' in Matlab). Note the strong non-stationarities in frequency. C) PPC spectrum shows a clear peak at the true mean frequency of 6 Hz. D) The phase histogram shows the phase derived from Wavelet analysis at 6 Hz. Mean angle of the spike phase is shown in blue, the ground truth phase angle is shown in red.

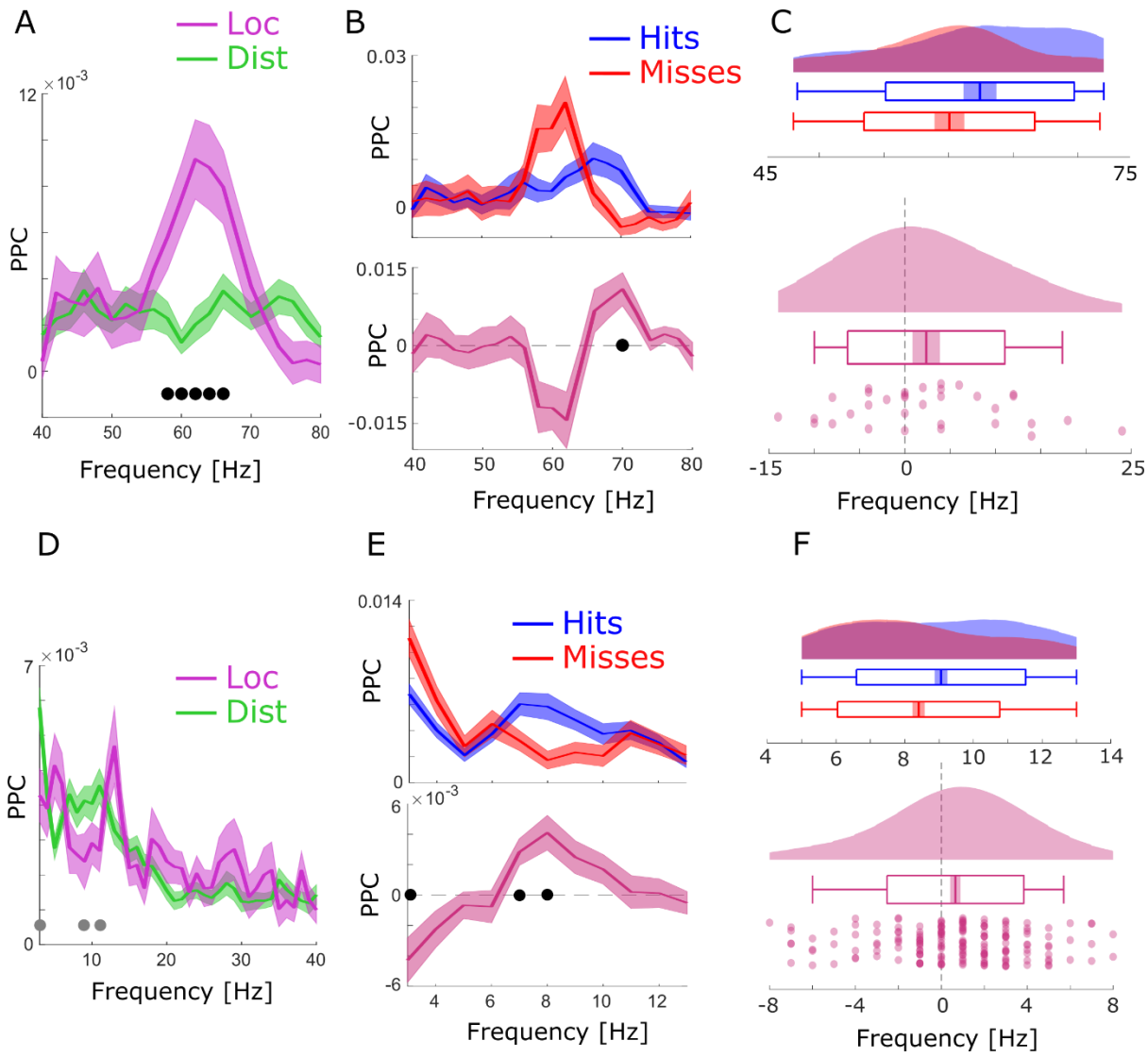

Fig S6. Spike-LFP coupling results obtained with bandpass filtering and Hilbert transformation.
A) Spike-LFP coupling for the high frequency range for local (pink) and distal (green) pairs is shown. Local spike-LFP pairs show higher phase coupling compared to distal pairs in the high gamma range (black dots; $p_{corr}<0.05$). B) Top: Spike-LFP coupling is shown for the gamma frequency range for local pairs only for hits (blue) and misses (red). Bottom: The difference between hits and misses is shown. Black dots indicate $p_{corr}<0.05$ (FDR corrected). C) Gamma peak frequency in PPC across all local spike-field pairs is shown for hits and misses (top), and for the difference (hits-misses). Box plots indicate the same indices as in Fig 3D in the main manuscript. Hits trend towards faster gamma frequencies compared to misses ($t_{32}=1.56$; $p=0.06$). D-F) Same as in A-C for the low frequency range. Hits and misses are shown for distal spike-LFP pairs only. Hits demonstrate significantly higher theta frequencies compared to misses ($t_{175}=2.73$; $p<0.005$).

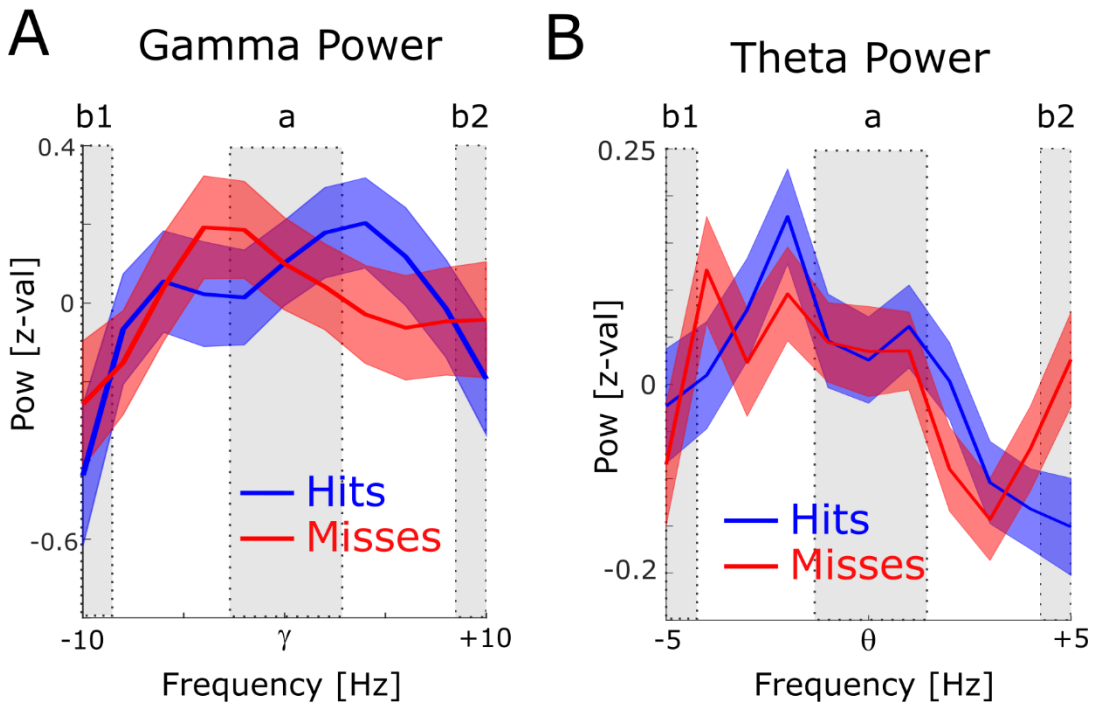

Fig. S7. Power for phase providing theta and gamma frequencies and PPC for high and low power spikes. A) The 1/f corrected power spectra are shown for hits (blue) and misses (red) centred on the peak gamma frequency of spike-LFP coupling. To demonstrate the existence of a meaningful signal in the phase providing frequency range (i.e. peak in the power spectrum) a paired samples t-test was calculated, where the power in the peak (a) was contrasted with the power at the edges (b1 and b2). Power values were averaged for hits and misses. For the gamma range, power at the peak was significantly higher compared to the power at the edges (t_{52}=2.38; $p<0.05$). B) Same as A but for the theta frequency range. Theta power at the peak was significantly higher compared to the power at the edges (t_{374}=2.44; $p<0.01$).

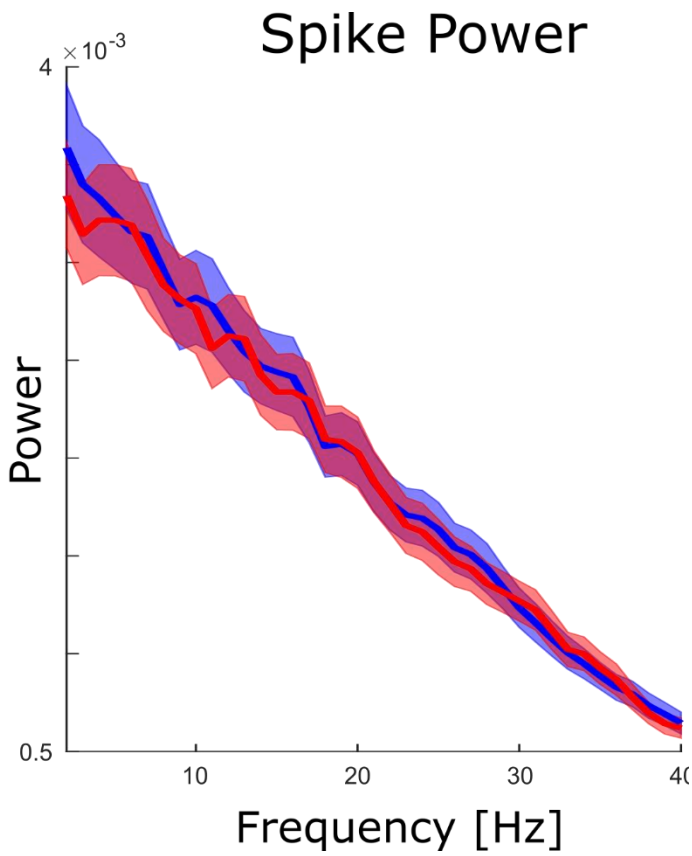

Fig. S8. Spike Power Analysis.

An FFT analysis is shown for continuous spike density time series to test whether spikes themselves showed clear peaks in the theta frequency range. No peaks were obtained neither for hits (blue) nor for misses (red), and no significant differences between hits and misses were observed ($p_{corr}>0.05$).

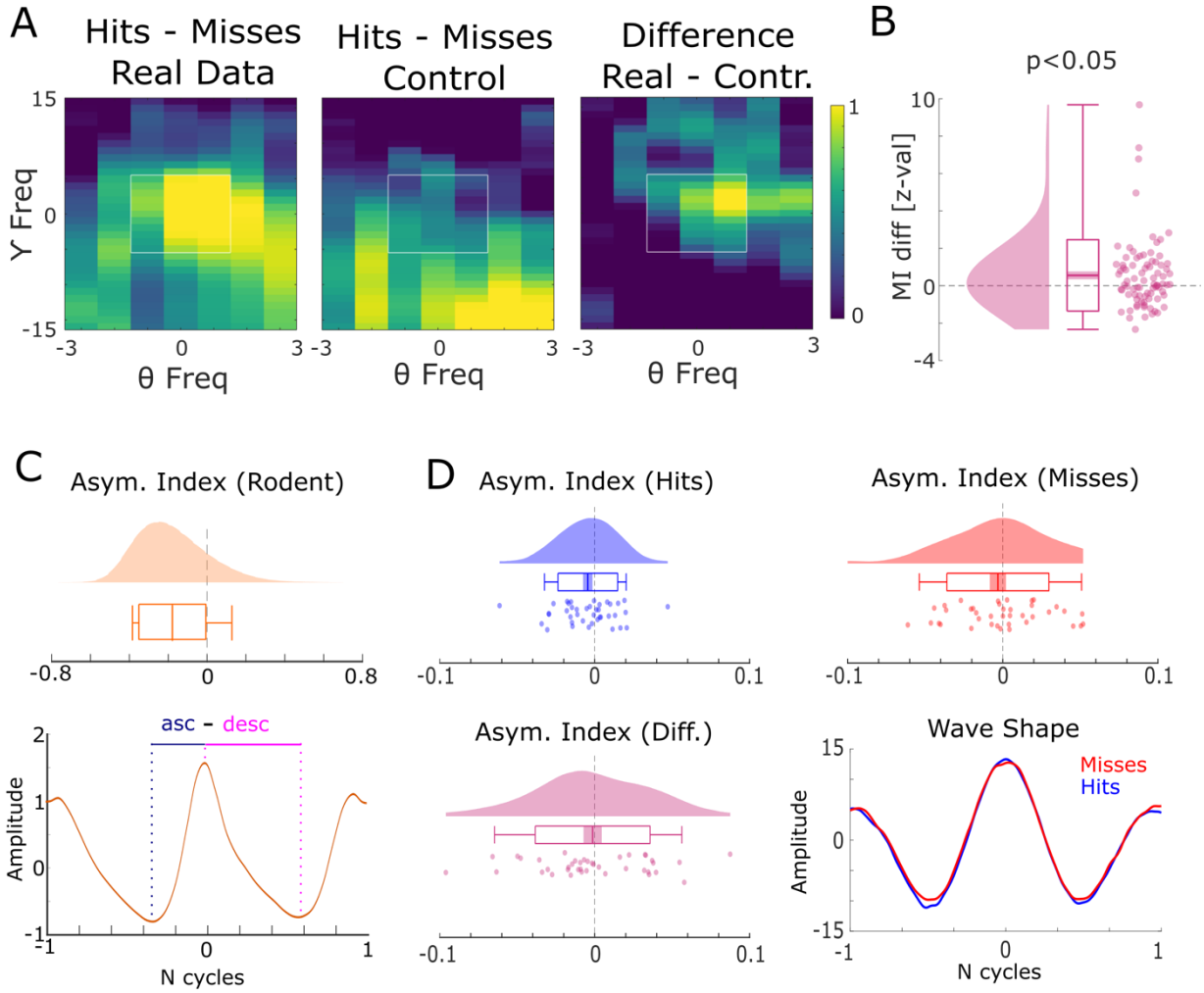

Fig. S9. Harmonic and asymmetric waveshape control analysis

A) The results of a harmonic control analysis are shown where the gamma power providing frequency was taken as the 8th harmonic of the theta phase providing frequency. The panel on the left shows the modulation index (MI) of the real data, the middle panel plots the MI from the harmonic control, and the panel on the right shows the difference. The white square highlights the window that was used for statistical analysis shown in (B). CFC for the real data is stronger than in the harmonic control data, ruling out an influence of asymmetric theta waveshapes. (C) Theta waveshape was quantified by the asymmetry index (see *(13)*) and is shown for a rodent LFP dataset recorded in the entorhinal cortex during an open field navigation task (courtesy of Ehren Newman). A strong asymmetry is present with the ascending flank covering less time than the descending flank. (D) The results of same analysis are shown for the theta providing channels in humans for hits (blue) and misses (red). Waveshapes appear much more symmetric compared to rodents (note the difference in scale on the x-axis between C and D), albeit both exhibit a slight asymmetry in the same direction as observed in rodents (ascending < descending flank). Importantly, no difference between hits and misses was observed in waveshape asymmetry, thus further ruling out an influence of asymmetric theta waveshape on the observed cross-frequency coupling results.

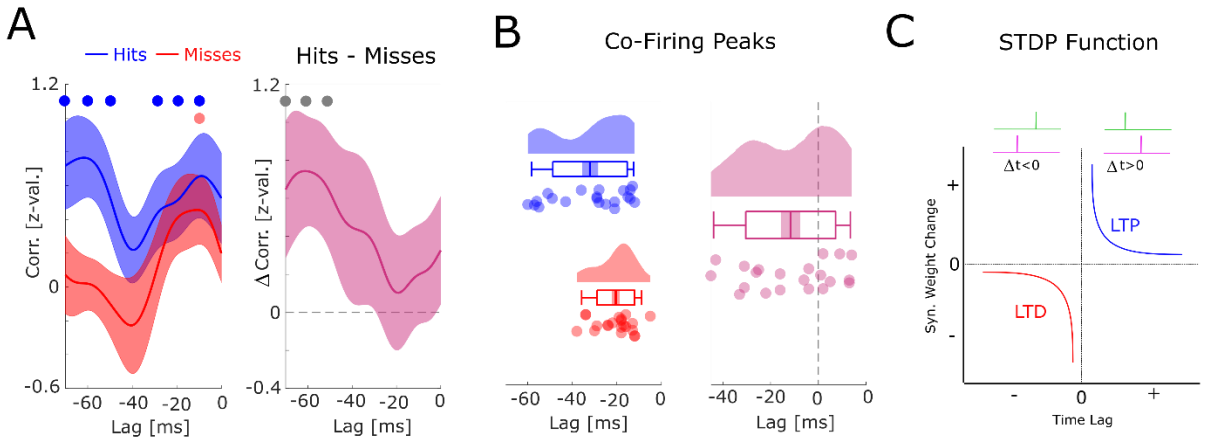

Fig. S10. Co-firing analysis at negative lags.
A) The results for the co-firing analysis at negative lags (putative down-stream neuron fires before putative up-stream neuron) are shown. Hits show significant above chance co-firings at lags -70 to -50, and -30 to -10 ms (p_{corr}<0.05), whereas misses show strongest co-firing only at lag -10 ms (p_{uncorr}<0.05). The co-firing difference between hits and misses is shown on the right, showing strongest differences at lags -60 to -40 ms (p_{uncorr}<0.05). B) Results of the co-firing peak detection analysis are plotted. Compared to hits, misses exhibit peak co-firings at shorter negative latencies (i.e. closer to 0; t_{20}=-2.82; p<0.05). C) A schematic of the STDP function is shown. Notably, the results shown in A and B, suggest that hits showed a tendency for putative down-stream neurons (pink) to fire *long* before putative up-stream neurons (green), whereas misses showed a tendency towards co-firing at a much *shorter* lag (-10 ms). This latter pattern would lead to a strong punishment of the synaptic connections (LTD), and hence weaker memories. Therefore, these results, albeit statistically weaker than the results for positive lags reported in the main manuscript (Figure 5), are fully consistent with STDP.

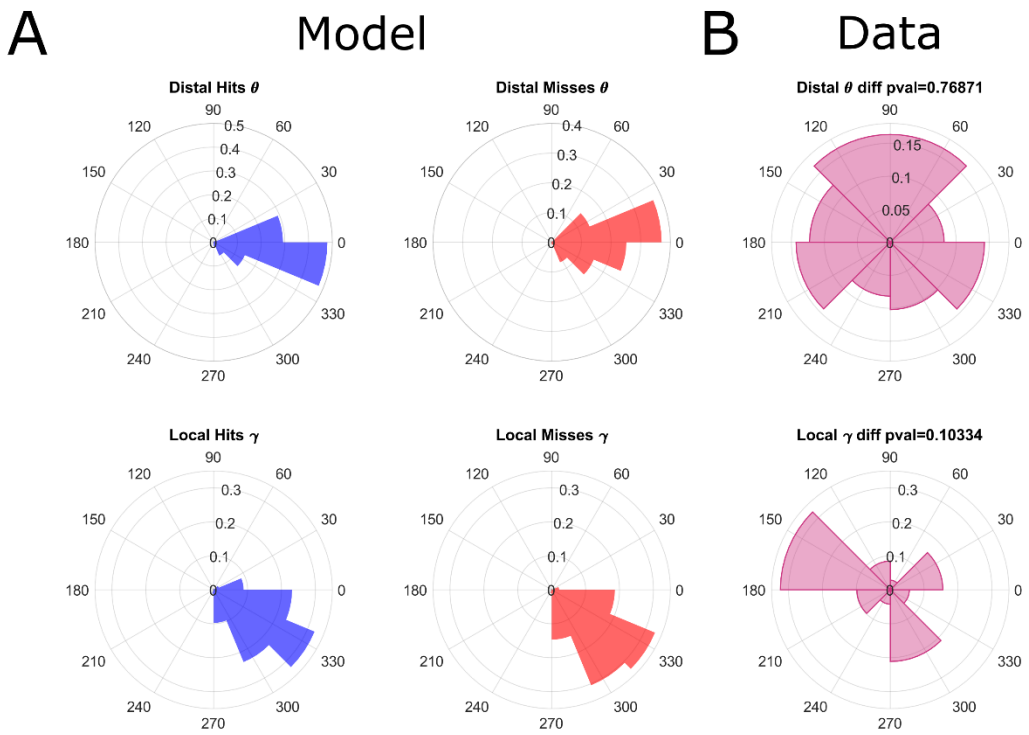

Fig. S11. Phase of firing for hits and misses for distal theta and local gamma.
A) The phase of firing is shown for neurons in the computational model for distally coupled theta neurons and locally coupled gamma neurons. Phase histograms show distribution of the phase at which neurons fire for hits (blue) and misses (red) for theta (top row) and gamma (bottom row). Both hits and misses fire at approximately the same phase. The slight discrepancy between hits and misses in the theta frequency (top panel) is due to phase advancement as a result of increasing weights over time for hits, however this slight difference cannot explain the difference in lag induced by frequency. B) Differences in phase of firing between hits and misses for the real data are shown for distally theta coupled neurons (top) and locally gamma coupled neurons (bottom). P values are reported from Raleigh tests that test for deviation from uniformity. No significant mean directions of phase differences between hits and misses were observed, neither for theta nor for gamma.

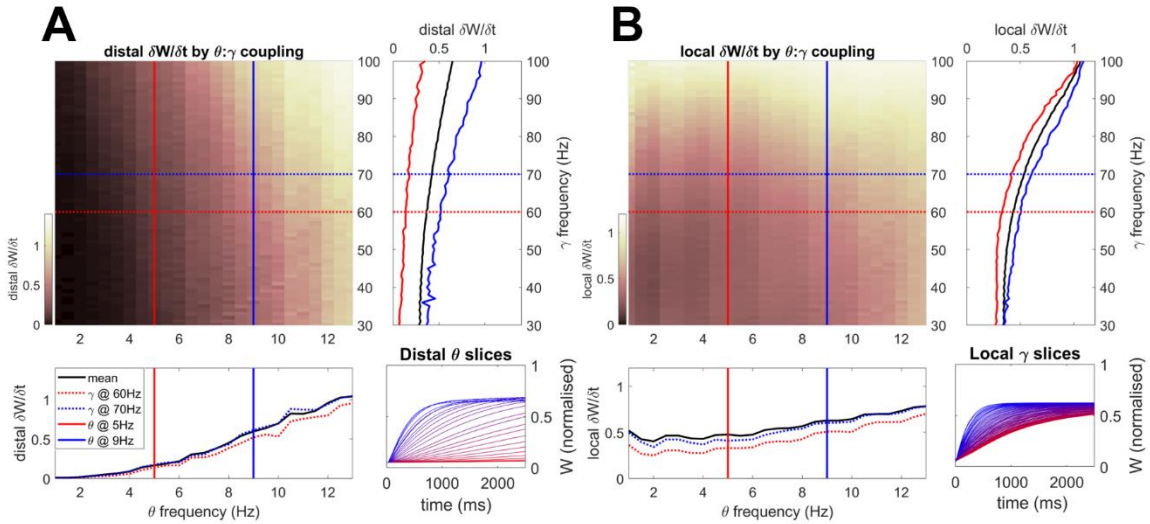

Fig. S12. Model shows how oscillatory frequency drives plasticity.

A) Theta (x-axis) frequency drives plasticity in distal-to-local synapses (z-axis), with slight interaction from gamma frequency (y-axis). Plasticity is calculated as the steepness of weight change over time, as illustrated in the bottom right-hand panel which plots distal-to-local weight change over time for each theta frequency (lows in reds, highs in blues), taking an average across all gamma frequencies. Bottom and side panels show plasticity averages across theta and gamma frequencies, respectively. Solid vertical red and blue lines indicate selected theta frequencies for "misses" & "hits," respectively. Dotted horizontal red and blue lines indicate selected gamma frequencies for "misses" & "hits," respectively. B) Gamma frequency drives plasticity in local-to-local synapses, with slight interaction from theta frequency. Bottom right-hand panel illustrates local-to-local weight change over time for each gamma frequency (lows in red, highs in blues), taking an average across all theta frequencies. We here assume full cross-frequency coupling for each frequency-by-frequency space (Equation 5; CFC = 1).

Supplementary Table S1: Regions where distally and locally coupled neurons were recorded

Patient IDs	Distally coupled (up-stream)	Locally coupled (down-stream)
P04	left mid. Hipp. MW4 N1	left EC MW3 N1
P04	left EC MW8 N1	left mid. Hipp. MW4 N1
P04	left mid. Hipp. MW7 N1	left EC MW3 N1
P05	left mid. Hipp. MW1 N1	right mid. Hipp. MW3 N1
P05	left mid. Hipp. MW5 N2	right mid. Hipp. MW3 N1
P07	left mid. Hipp. MW8 N1	right ant. Hipp. MW6 N1
P07	right mid. Hipp. MW4 N1	right ant. Hipp. MW6 N1
P07	right ant. Hipp. MW4 N1	right mid. Hipp. MW2 N2
P07	right ant. Hipp. MW7 N1	right mid. Hipp. MW2 N2
P07	right mid. Hipp. MW3 N2	right ant. Hipp. MW7 N2
P07	right mid. Hipp. MW4 N1	right ant. Hipp. MW7 N2
P08	left ant. Hipp. MW1 N1	right mid. Hipp. MW8 N1
P08	left ant. Hipp. MW3 N1	right mid. Hipp. MW8 N1
P08	left ant. Hipp. MW5 N1	right mid. Hipp. MW8 N1
P08	left ant. Hipp. MW8 N1	right mid. Hipp. MW8 N1
P08	left ant. Hipp. MW3 N1	right mid. Hipp. MW2 N1
P08	left ant. Hipp. MW3 N1	right mid. Hipp. MW1 N1
P08	right mid. Hipp. MW1 N1	left ant. Hipp. MW3 N1
P08	right mid. Hipp. MW1 N1	left ant. Hipp. MW8 N1
P09	left ant. Hipp. MW7 N1	right mid. Hipp. MW6 N1
P09	left PHC MW6 N1	right mid. Hipp. MW6 N1
P09	right post. Hipp. MW2 N1	right mid. Hipp. MW6 N1
P09	right post. Hipp. MW5 N1	right mid. Hipp. MW6 N1
P09	left PHC MW5 N1	right mid. Hipp. MW4 N1

EC = entorhinal Cortex; ant. = anterior; mid = middle; post. = posterior; Hipp. = Hippocampus; PHC = parahippocampal cortex; MW = Microwire on which neuron was recorded; N = cluster ID as obtained by WaveClus ;

Supplementary References

1. E. R. Kandel, The molecular biology of memory storage: a dialogue between genes and synapses. *Science* **294**, 1030-1038 (2001).
2. H. Markram, J. Lubke, M. Frotscher, B. Sakmann, Regulation of synaptic efficacy by coincidence of postsynaptic APs and EPSPs. *Science* **275**, 213-215 (1997).
3. G. Bi, M. Poo, Synaptic modification by correlated activity: Hebb's postulate revisited. *Annu Rev Neurosci* **24**, 139-166 (2001).
4. D. O. Hebb, *The organization of behavior; a neuropsychological theory*. A Wiley book in clinical psychology (Wiley, New York,, 1949), pp. xix, 335 p.
5. V. Wespatat, F. Tennigkeit, W. Singer, Phase sensitivity of synaptic modifications in oscillating cells of rat visual cortex. *J Neurosci* **24**, 9067-9075 (2004).
6. G. Buzsaki, Neural syntax: cell assemblies, synapsembles, and readers. *Neuron* **68**, 362-385 (2010).
7. P. Fries, Rhythms for Cognition: Communication through Coherence. *Neuron* **88**, 220-235 (2015).
8. W. Singer, Neuronal synchrony: a versatile code for the definition of relations? *Neuron* **24**, 49-65, 111-125 (1999).
9. W. Penfield, B. Milner, Memory deficit produced by bilateral lesions in the hippocampal zone. *AMA Arch Neurol Psychiatry* **79**, 475-497 (1958).
10. J. Fell, N. Axmacher, The role of phase synchronization in memory processes. *Nat Rev Neurosci* **12**, 105-118 (2011).
11. M. J. Jutras, E. A. Buffalo, Synchronous neural activity and memory formation. *Curr Opin Neurobiol* **20**, 150-155 (2010).
12. P. T. Huerta, J. E. Lisman, Bidirectional synaptic plasticity induced by a single burst during cholinergic theta oscillation in CA1 in vitro. *Neuron* **15**, 1053-1063 (1995).
13. J. M. Hyman, B. P. Wyble, V. Goyal, C. A. Rossi, M. E. Hasselmo, Stimulation in hippocampal region CA1 in behaving rats yields long-term potentiation when delivered to the peak of theta and long-term depression when delivered to the trough. *J Neurosci* **23**, 11725-11731 (2003).
14. U. Rutishauser, I. B. Ross, A. N. Mamelak, E. M. Schuman, Human memory strength is predicted by theta-frequency phase-locking of single neurons. *Nature* **464**, 903-907 (2010).
15. B. Griffiths *et al.*, Directional coupling of slow and fast hippocampal gamma with neocortical alpha/beta oscillations in human episodic memory. *Proc Natl Acad Sci U S A* **in press**, (2019).
16. J. F. Burke, A. G. Ramayya, M. J. Kahana, Human intracranial high-frequency activity during memory processing: neural oscillations or stochastic volatility? *Curr Opin Neurobiol* **31**, 104-110 (2015).
17. G. Buzsaki, E. W. Schomburg, What does gamma coherence tell us about inter-regional neural communication? *Nat Neurosci* **18**, 484-489 (2015).
18. S. Liebe, G. M. Hoerzer, N. K. Logothetis, G. Rainer, Theta coupling between V4 and prefrontal cortex predicts visual short-term memory performance. *Nat Neurosci* **15**, 456-462, S451-452 (2012).
19. S. N. Jacob, D. Hahnke, A. Nieder, Structuring of Abstract Working Memory Content by Fronto-parietal Synchrony in Primate Cortex. *Neuron* **99**, 588-597 e585 (2018).
20. M. Vinck, M. van Wingerden, T. Womelsdorf, P. Fries, C. M. Pennartz, The pairwise phase consistency: a bias-free measure of rhythmic neuronal synchronization. *Neuroimage* **51**, 112-122 (2010).
21. D. Bush, N. Burgess, Advantages and detection of phase coding in the absence of rhythmicity. *Hippocampus* **30**, 745-762 (2020).
22. T. Eliav *et al.*, Nonoscillatory Phase Coding and Synchronization in the Bat Hippocampal Formation. *Cell* **175**, 1119-1130 e1115 (2018).
23. A. B. Tort, R. Komorowski, H. Eichenbaum, N. Kopell, Measuring phase-amplitude coupling between neuronal oscillations of different frequencies. *J Neurophysiol* **104**, 1195-1210 (2010).
24. J. Aru *et al.*, Untangling cross-frequency coupling in neuroscience. *Curr Opin Neurobiol* **31**, 51-61 (2015).
25. D. H. Brainard, The psychophysics toolbox. *Spatial vision* **10**, 433-436 (1997).
26. R. Q. Quiroga, Z. Nadasdy, Y. Ben-Shaul, Unsupervised spike detection and sorting with wavelets and superparamagnetic clustering. *Neural Comput* **16**, 1661-1687 (2004).
27. M. J. Ison, R. Quian Quiroga, I. Fried, Rapid Encoding of New Memories by Individual Neurons in the Human Brain. *Neuron* **87**, 220-230 (2015).

28. J. Jacobs, M. J. Kahana, A. D. Ekstrom, I. Fried, Brain oscillations control timing of single-neuron activity in humans. *J Neurosci* **27**, 3839-3844 (2007).
29. R. Oostenveld, P. Fries, E. Maris, J. M. Schoffelen, FieldTrip: Open source software for advanced analysis of MEG, EEG, and invasive electrophysiological data. *Comput Intell Neurosci* **2011**, 156869 (2011).
30. J. F. Hipp, D. J. Hawellek, M. Corbetta, M. Siegel, A. K. Engel, Large-scale cortical correlation structure of spontaneous oscillatory activity. *Nat Neurosci* **15**, 884-890 (2012).
31. Y. Benjamini, Y. Hochberg, Controlling the False Discovery Rate - a Practical and Powerful Approach to Multiple Testing. *J R Stat Soc B* **57**, 289-300 (1995).
32. G. Nolte *et al.*, Robustly estimating the flow direction of information in complex physical systems. *Phys Rev Lett* **100**, 234101 (2008).
33. P. B. Sederberg *et al.*, Hippocampal and neocortical gamma oscillations predict memory formation in humans. *Cereb Cortex* **17**, 1190-1196 (2007).
34. J. F. Burke *et al.*, Synchronous and asynchronous theta and gamma activity during episodic memory formation. *J Neurosci* **33**, 292-304 (2013).
35. M. A. Belluscio, K. Mizuseki, R. Schmidt, R. Kempter, G. Buzsaki, Cross-frequency phase-phase coupling between theta and gamma oscillations in the hippocampus. *J Neurosci* **32**, 423-435 (2012).
36. J. Niediek, J. Bostrom, C. E. Elger, F. Mormann, Reliable Analysis of Single-Unit Recordings from the Human Brain under Noisy Conditions: Tracking Neurons over Hours. *PLoS One* **11**, e0166598 (2016).